J. Fluid Mech. (2025), *vol.* 1009, A36, doi:10.1017/jfm.2025.240

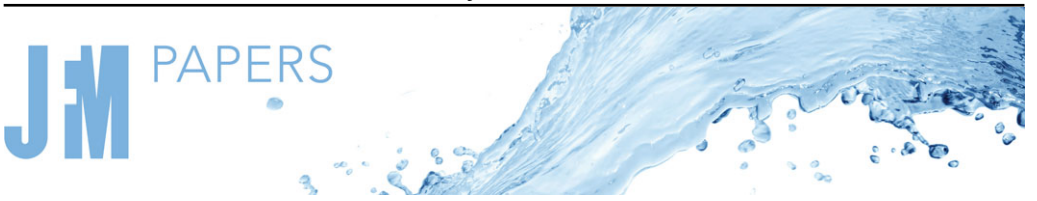

Prediction of flow and polymeric stresses in a viscoelastic turbulent channel flow using convolutional neural networks

Arivazhagan G. Balasubramanian[1,2], **Ricardo Vinuesa**[1,2] and **Outi Tammisola**[1,2]

[1]FLOW, Dept. Engineering Mechanics, KTH Royal Institute of Technology, Stockholm 100 44, Sweden

[2]Swedish e-Science Research Centre (SeRC), Stockholm, Sweden

Corresponding author: Arivazhagan G. Balasubramanian, argb@mech.kth.se

(Received 16 August 2024; revised 13 February 2025; accepted 22 February 2025)

Neural network models have been employed to predict the instantaneous flow close to the wall in a viscoelastic turbulent channel flow. Numerical simulation data at the wall are used to predict the instantaneous velocity fluctuations and polymeric-stress fluctuations at three different wall-normal positions in the buffer region. Such an ability of non-intrusive predictions has not been previously investigated in non-Newtonian turbulence. Our comparative analysis with reference simulation data shows that velocity fluctuations are predicted reasonably well from wall measurements in viscoelastic turbulence. The network models exhibit relatively improved accuracy in predicting quantities of interest during the hibernation intervals, facilitating a deeper understanding of the underlying physics during low-drag events. This method could be used in flow control or when only wall information is available from experiments (for example, in opaque fluids). More importantly, only velocity and pressure information can be measured experimentally, while polymeric elongation and orientation cannot be directly measured despite their importance for turbulent dynamics. We therefore study the possibility to reconstruct the polymeric-stress fields from velocity or pressure measurements in viscoelastic turbulent flows. The neural network models demonstrate a reasonably good accuracy in predicting polymeric shear stress and the trace of the polymeric stress at a given wall-normal location. The results are promising, but also underline that a lack of small scales in the input velocity fields can alter the rate of energy transfer from flow to polymers, affecting the prediction of the polymeric-stress fluctuations.

Key words: machine learning, viscoelasticity, turbulence simulation

1. Introduction

Viscoelastic fluids are widely used in industrial processes and an understanding of complex-fluid behaviour becomes crucial for enterprises working with non-Newtonian flows. Further, in real-world scenarios, turbulent flows predominate, exhibiting chaotic and multi-scale dynamics. The turbulent flows of purely viscoelastic fluids have important technological implications due to increased mixing efficiencies at low Reynolds numbers and have also piqued the interest in drag reduction and flow control communities at high Reynolds numbers. The addition of a tiny amount of polymer (parts per million) has proven efficient in reducing friction drag in pipe flows (Virk 1971), leading to substantial energy savings in fluid-transport applications. Such observation sparked intense research into the interaction between flow dynamics and polymers, in the context of skin-friction reduction. Lumley (1969) postulated that the drag reduction attributed to polymer molecules arises from the extension of polymers, thereby increasing the effective extensional viscosity of the solution. This increase in extensional viscosity leads to the damping of small eddies, resulting in increased buffer layer thickness. However, De Gennes (1986) attributed the drag reduction to elastic effects rather than the viscous properties of polymers. This theory assumes that the turbulent kinetic energy (TKE) is stored as elastic energy by the polymers, thereby influencing the energy cascade. Nevertheless, neither theory offers a comprehensive description of polymer-induced drag reduction.

Various experimental investigations in channel and pipe flows (Pinho & Whitelaw 1990; Wei & Willmarth 1992; Den Toonder *et al.* 1997; Warholic, Massah & Hanratty 1999, 2001; Ptasinski *et al.* 2001, 2003) have shown that polymers induce changes in the turbulence structure rather than simply attenuating it. These changes are characterised by an increase in streamwise turbulence intensity alongside a decrease in wall-normal fluctuations. With access to direct numerical simulation (DNS) techniques (Sureshkumar, Beris & Handler 1997), a deeper insight into the intricate interaction between polymers and flow fields has been probed. Notably, Dubief *et al.* (2004, 2005) pointed out that the polymers exhibited a structured energy exchange with the flow, primarily occurring around near-wall vortices. This increased polymer activity in the buffer region suggests that polymers are entrained around the vortices, resulting in the torque due to polymeric stress opposing the rotation of the streamwise vortices (Kim *et al.* 2007), thereby extracting energy from near-wall vortices. Consequently, polymer stretching weakens the near-wall coherent structures, leading to a reduction of skin friction (Stone, Waleffe & Graham 2002; Dubief *et al.* 2004; Li & Graham 2007; Kim *et al.* 2007, 2008). In addition to damping near-wall vortices, polymers also enhance the streamwise kinetic energy in near-wall streaks, thereby the net balance of these gives rise to a self-sustained drag-reduced turbulent flow (Dubief *et al.* 2004, 2005). Furthermore, Xi & Graham (2010, 2012) suggested that the turbulent flow is characterised by an alternating sequence of active and hibernating phases. These phases are distinguished by flow structures exhibiting strong vortices and wavy streaks during the active phase, and weak streamwise vortices during the hibernation phase, with viscoelastic flows characterised by increased hibernation intervals. Additional insights into the influence of polymer additives on drag reduction are detailed by Xi (2019).

Overall, the studies indicate that drag reduction caused by polymer molecules arises from their complex and dynamic interactions with turbulent flow structures. Nonetheless, the exact behaviour of polymers in turbulent flows remains an open question. Moreover, the intermittent dynamics near the wall are primarily explored using numerical simulations, as they provide direct access to polymeric-stress fields through constitutive

equations for viscoelastic fluids. In contrast, experimental investigations of drag reduction in viscoelastic flows are limited by the challenges of near-wall measurements and the inability of current techniques to directly measure polymeric stress (Stone & Graham 2003). Consequently, while direct measurements of polymeric stress in experiments are not feasible, flow fields measurable through experimental techniques can serve as inputs to machine-learning models to infer polymeric-stress fields indirectly. This approach represents a promising avenue for gaining insights into polymeric-stress dynamics in turbulent flows and bridging the gap between numerical and experimental investigations. Since a complete description of viscoelastic turbulence would require characterisation of both velocity and polymeric stresses, a deeper understanding of viscoelastic turbulence would benefit from advances in methodologies that combine experimental measurements of velocity fields with computational models to infer stress distributions (Thakur, Raissi & Ardekani 2024).

The phenomenon of drag reduction in viscoelastic turbulent flows has been explored from theoretical, experimental and numerical perspectives. However, in recent years, machine-learning methods have expanded the possibilities in simulating (Raissi, Yazdani & Karniadakis 2020; Eivazi *et al.* 2022; Vinuesa & Brunton 2022), predicting (Eivazi *et al.* 2021; Guastoni *et al.* 2021; Yousif *et al.* 2023*a*,*b*) and controlling (Guastoni *et al.* 2023; Vignon, Rabault & Vinuesa 2023) wall-bounded Newtonian turbulent flows (Vinuesa 2024). Data-driven methods also hold potential for enhancing the understanding of the role of coherent structures in Newtonian (Cremades *et al.* 2024) and viscoelastic turbulence dynamics (Le Clainche *et al.* 2020). In viscoelastic turbulence, Kumar, Constante-Amores & Graham (2025) demonstrated that low-dimensional models of elastoinertial turbulence (EIT), obtained by combining proper-orthogonal decomposition (POD), autoencoders and neural ordinary differential equations (NODEs), can accurately capture short and long-term dynamics of dilute polymer solutions thereby significantly reducing computational costs. In the domain of polymeric stress predictions, researchers have explored the predictability of polymeric-stress components from velocity gradient using neural networks (Nagamachi & Tsukahara 2019) and have also developed a framework for rheological model discovery from the velocity field and information corresponding to boundary conditions and initial condition of polymeric stress (Thakur *et al.* 2024). These examples underscore the possibilities offered by data-driven methods to advance the understanding of polymers and flow field interaction in viscoelastic turbulent flow. However, a critical first step is to estimate the instantaneous polymer behaviour in an experimental setting. But, experimental studies encounter difficulties in accurately quantifying macromolecular extension, thereby significantly restricting the ability to fully characterise polymer behaviour (Stone & Graham 2003). Moreover, near-wall measurements of flow fields in turbulent channel flows can also pose challenges. Nevertheless, nonlinear machine-learning tools offer possibilities for improving experimental flow measurements and estimating flow and scalar quantities (Vinuesa, Brunton & McKeon 2023; Eivazi *et al.* 2024). Neural network models and, in particular, fully convolutional network (FCN) models have demonstrated excellent capabilities in predicting the instantaneous state of the flow using quantities measured at the wall in Newtonian turbulent flow (Guastoni *et al.* 2021).

Hence, in the present study, the idea of non-intrusive sensing has been applied to viscoelastic turbulent channel flow to predict the velocity fluctuations and polymeric-stress components near the wall using the quantities measured at the wall. To this end, FCN models are employed to predict the two-dimensional velocity fluctuations and polymeric-stress-fluctuation fields at different wall-normal distances. The obtained predictions from FCN models are compared with reference simulation data and the analysis indicates that

velocity fluctuations can be reasonably well predicted in viscoelastic turbulence similar to the results obtained by Guastoni *et al.* (2021) for Newtonian wall-bounded turbulent flow. Further, the present work highlights that the errors between reference fields and predictions are lower in hibernation intervals in comparison to those at high-shear events, highlighting the ability of the network model to relatively well capture the underlying physics at low-drag events. Thus, the present work highlights the capability of a data-driven approach to model turbulence in complex-fluid flows. As a first step, directly providing a possible experimental measurement of wall quantities or near-wall velocity fluctuations as inputs to the network model allows for an estimation of the polymeric-stress quantities in the near-wall region from experimental observations. Furthermore, the developed non-intrusive sensing models will also find useful applications in closed-loop control of wall-bounded turbulence in viscoelastic flows.

The paper is organised as follows. The methodology employed in the present work is introduced in § 2. A description on the dataset to train the network models is provided in § 2.1 and an overview of the network models can be found in § 2.2. A filter-based approach to identify the effects of small scales on FCN predictions is detailed in § 2.3. In § 3, the results obtained with different network models are discussed. The performance of the network models in different prediction types is outlined in §§ 3.1–3.3. The effects of filtering the small scales in the input velocity fluctuations on the predictions by FCN is discussed in §§ 3.4 and 3.5, and an interpretation of the predictions by FCN is provided in § 3.6. Additional details regarding the error metrics for different types of predictions and the analysis of predictions of polymeric shear stress can be found in Appendices A–C.

2. Methodology

2.1. *Dataset*

To estimate the turbulent dynamics of the viscoelastic fluid from velocity fields, direct numerical simulation of viscoelastic turbulent channel flow is performed to generate the data necessary for modelling the relationship between near-wall velocity fluctuations and polymeric-stress-fluctuation quantities of interest using a fully convolutional neural network model. For the direct numerical simulation, a macroscopic continuum description of fluid–polymer interaction is considered. Specifically, an homogeneous dilute mixture of polymer in the solvent fluid is modelled with the finitely extensible nonlinear elastic with Peterlin closure (FENE-P) constitutive relation (refer to (2.4)). Although more sophisticated models (Watanabe & Gotoh 2014; Shen *et al.* 2022) could be considered, Stone & Graham (2003) demonstrated that the FENE-P model can still yield reasonable predictions of the spatial distribution of stresses due to polymers and indicated that while the transient extension for the FENE-P model compares favourably to a more detailed model such as bead-spring-chain models, it may overestimate elastic stresses in turbulent flow. The FENE-P model still remains by far the most widely used option for investigating viscoelastic turbulence and drag reduction phenomena owing to its ability to reproduce essential features of polymer dynamics such as polymer drag reduction, including the maximum-drag reduction asymptote (Graham 2014). Dubief *et al.* (2022, 2023) also highlight its role in studies of EIT, a chaotic state driven by polymer dynamics, and for understanding elastic turbulence and maximum drag reduction. Hence, in the present study, FENE-P model is used with the notion that it accurately describes the polymer physics of the considered viscoelastic liquid.

In the macroscopic description of the polymer model, we consider the statistics of end-to-end vector $\mathbf{R}$ to characterise the average of the end-to-end vectors of a large number of

polymer macro-molecules contained in a fluid particle. An essential statistical quantity in this description is the second-order correlation of the orientation vector $\mathbf{R}$, known as the conformation tensor ($\mathbf{A}$) which is obtained by

$$\mathbf{A} = \frac{A_{ij}}{R_0^2} = \frac{\langle R_i R_j \rangle_f}{R_0^2}, \tag{2.1}$$

where $\langle \cdot \rangle_f$ corresponds to the statistical average over a fluid particle and R_0^2 corresponds to the root mean square (r.m.s.) of all the end-to-end vectors inside a fluid particle at rest.

The dimensional incompressible Navier–Stokes equations coupled with the evolution equation for the polymer conformation tensor are given by

$$\frac{\partial \boldsymbol{u}}{\partial t} + (\boldsymbol{u} \cdot \nabla \boldsymbol{u}) = -\frac{1}{\rho}\nabla p + \frac{\mu_s}{\rho}\nabla^2 \boldsymbol{u} + \left[\frac{\mu_p}{\rho\lambda}\nabla \cdot (\mathcal{P}(\mathbf{A})\mathbf{A})\right], \tag{2.2}$$

$$\nabla \cdot \mathbf{u} = 0, \tag{2.3}$$

$$\frac{\partial \mathbf{A}}{\partial t} + \boldsymbol{u} \cdot \nabla \mathbf{A} = \mathbf{A} \cdot \nabla \boldsymbol{u} + (\nabla \boldsymbol{u})^T \cdot \mathbf{A} - \frac{1}{\lambda}\left[\mathcal{P}(\mathbf{A})\mathbf{A} - \mathbf{I}\right], \tag{2.4}$$

$$\mathcal{P}(\mathbf{A}) = \frac{L_{max}^2}{L_{max}^2 - \mathrm{tr}(\mathbf{A})} \tag{2.5}$$

where $\boldsymbol{u}$ is the velocity with corresponding components in streamwise, wall-normal and spanwise directions represented by u, v, w, and p is the pressure. In the remainder of the text, the instantaneous quantities are expressed as the sum of a mean component – obtained by averaging over space and time – and a fluctuating component. Consequently, the mean velocity components are denoted by $\langle U \rangle$, $\langle V \rangle$, $\langle W \rangle$ and the corresponding fluctuations by u, v, w. In (2.2), ρ is the density of the fluid with t denoting the time and λ denoting the relaxation time scale of polymeric stress. The solvent and polymer viscosity of the fluid are given by μ_s, μ_p, respectively, and they depend on the polymer concentration. The Peterlin function $\mathcal{P}(\mathbf{A})$ accounts for the finite length of the polymer molecules with L_{max} denoting the upper limit of the normalised polymer extension length, the point after which the polymers cannot absorb more energy from the flow.

The polymeric stress $\boldsymbol{\tau_p}$ can be retrieved from the conformation tensor using the Kramer relationship:

$$\boldsymbol{\tau_p} = \frac{\mu_p}{\lambda}\left(\mathbf{A} - \mathbf{I}\right). \tag{2.6}$$

Note that the mean of the polymeric-stress component is obtained by averaging in space and time, and is denoted by $\langle \tau_{p,\mathrm{ij}} \rangle$ and the corresponding fluctuation by $\tau_{p,\mathrm{ij}}$. Alternatively, one could also obtain the polymeric-stress components by predicting the conformation tensor and thereby retrieve the required stress components, in which case, one can employ geometric decomposition of conformation tensor as introduced by Hameduddin *et al.* (2018) (see also Hameduddin, Gayme & Zaki 2019; Hameduddin & Zaki 2019). This approach presents an interesting avenue for future work. However, in the present study, we aim to directly predict the fluctuation components of polymeric-stress components of interest from input fields and, hence, we consider the above-described decomposition of polymeric-stress components. Further, it should be highlighted that one of the difficulties in simulating viscoelastic fluid flow comes from the preservation of positive definiteness of the conformation tensor ($\mathbf{A}$) during the evolution of turbulent flow at high Weissenberg number ($Wi := \lambda U_b / h$, with U_b corresponding to the bulk velocity and h is the channel half-height; Wi quantifies the elastic forces with respect to the viscous forces, thereby

indicating the degree of anisotropy in the flow). Sureshkumar & Beris (1995) used artificial diffusion with the hyperbolic polymer evolution equation. The artificial diffusion can be either local (Dubief *et al.* 2004, 2005) or global (Sureshkumar *et al.* 1997). Despite the simplicity of the method, artificial diffusion affects the dynamics of the polymers at the small scales (Nguyen *et al.* 2016; Yerasi *et al.* 2024). Therefore, in the present study, the log-conformation approach (Fattal & Kupferman 2004) is used to ensure the positive definiteness of the conformation tensor and thereby circumvent the high-Weissenberg-number problem. However, it does not alter the inherent hyperbolic nature of the governing equations, thereby imposing stringent demands on mesh refinement and significantly increasing the associated computational costs. While the log-conformation transformation circumvents the issue of the loss of positive definiteness in the polymer conformation tensor, it does not eliminate the hyperbolic nature of the governing equations and poses stringent requirements in terms of mesh refinement levels and the associated computational costs. The advection of the log-conformation tensor is performed using the WENO5 scheme for its ability to accurately capture sharp gradients and discontinuities with minimal spurious oscillations. The time advancement of the conformation tensor is performed using a third-order Runge–Kutta (RK3) scheme. More details on the numerical methodology can be found from Rosti *et al.* (2018) and Izbassarov *et al.* (2021). Furthermore, the wall fields (see figure 4*a*) can exhibit high-frequency structures, which may be associated with the polymer diffusive instabilities as highlighted by Beneitez, Page & Kerswell (2023), Couchman *et al.* (2024) and Beneitez *et al.* (2024). These structures could potentially stem from the inherent numerical diffusion in solving the polymeric stress equations, as no artificial diffusivity is employed in the present numerical simulations.

The dataset for training and evaluation of the network model is obtained through a DNS of turbulent channel flow of viscoelastic fluid at a Reynolds number based on the bulk velocity of $Re = U_b h/\nu = 2800$ ($\nu = (\mu_s + \mu_p)/\rho$ denotes the total kinematic viscosity of the fluid), which corresponds to a friction Reynolds number $Re_\tau = 180$ (where Re_τ is defined in terms of h and friction velocity u_τ) for a Newtonian fluid. In this study, the turbulent channel flow simulations are performed at a Weissenberg number $Wi = 8$. The ratio of polymeric viscosity (μ_p) to the total viscosity ($\mu_s + \mu_p$), which is denoted by α, is set to 0.1. The maximum polymer extensibility is set to $L_{max} = 60$. The difficulties associated with proper rheological characterisation of real fluids by adequate constitutive equations is an important area of research on its own and rather, we assume that the adopted model adequately describes the intended fluid properties.

The viscoelastic turbulent channel flow is simulated using a finite-difference-based in-house code on a computational domain of size $6h \times 2h \times 3h$ in the streamwise (x), wall-normal (y) and spanwise directions (z), respectively, as shown in figure 1. The readers are referred to Izbassarov *et al.* (2021) for a complete description of the viscoelastic turbulent channel simulation employed in this study. The computational domain is uniformly discretised using $1728 \times 576 \times 864$ grid points along x, y and z, respectively. A spatial resolution of $\Delta x^+ = \Delta y^+ = \Delta z^+ < 0.6$ is chosen to fully resolve the turbulent scales in the viscoelastic turbulent flow (see also Rosti *et al.* 2018; Izbassarov *et al.* 2021). Here, the superscript '+' denotes the scaling in terms of the friction velocity u_τ ($= \sqrt{\tau_w/\rho}$, where τ_w corresponds to the wall-shear stress) and viscous length $\ell^* (= \nu/u_\tau)$. Note that the value of u_τ obtained with $Wi = 8$ is lower than that in the Newtonian case ($u_\tau \approx 180/Re_b$; since $Re_{\tau,\, Wi=0} \approx 180$) due to skin-friction reduction (refer also to mean velocity profile plotted in figure 3). Variation of the averaged wall-shear rate ($\langle U_y \rangle_{x,z}|_{\text{wall}}$) obtained with $Wi = 8$ is compared against the Newtonian case ($Wi = 0$) in figure 2. Here, U_y corresponds to the wall-normal derivative of the streamwise velocity and $\langle \cdot \rangle_{x,z}$ denotes

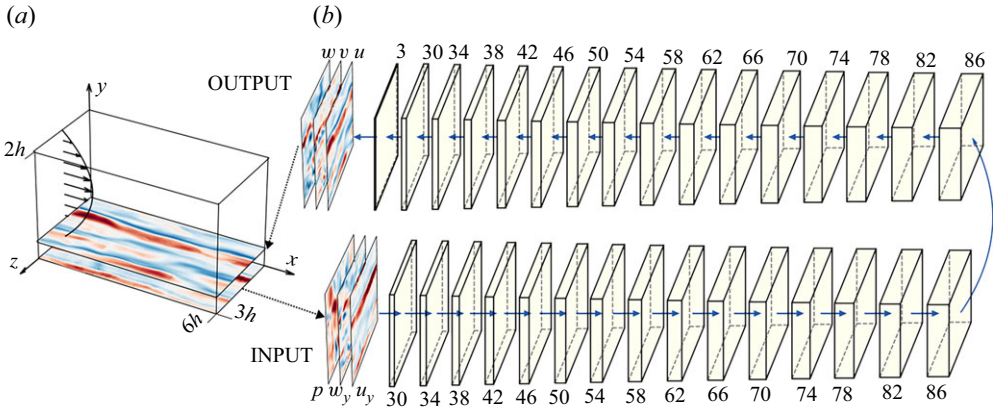

Figure 1. Typical workflow representation of V-prediction using fully convolutional network (FCN) model. (*a*) The computational domain for the channel flow and (*b*) FCN model with the corresponding number of kernels in each hidden layer indicated.

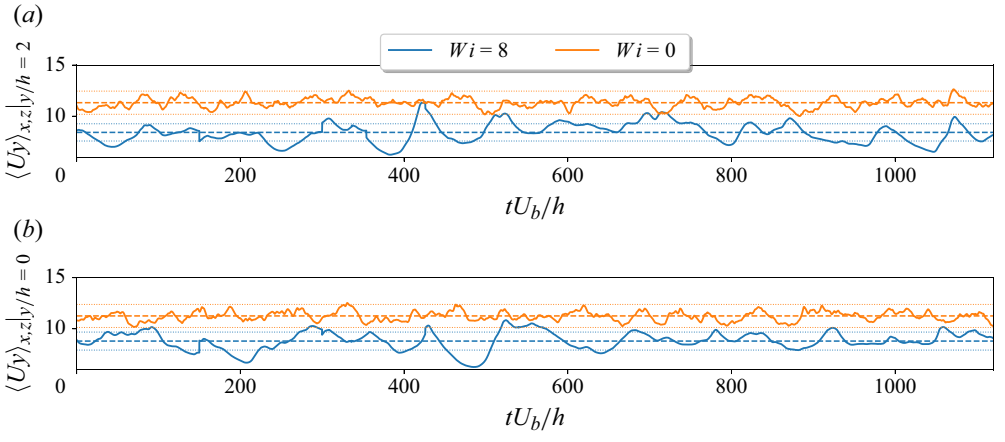

Figure 2. Time evolution of the wall-shear rate in a viscoelastic channel flow corresponding to $Wi = 8$ and Newtonian channel flow ($Wi = 0$) at (*a*) $y/h = 2$ and (*b*) $y/h = 0$. The dashed lines indicate the temporal mean and the dotted lines indicate the 10 % deviation from the temporal mean.

the spatial averaging in x and z directions in the channel. From figure 2, identifying the hibernation intervals (regions with low wall-shear stress) using area-averaged wall-shear rate as performed by Xi & Graham (2010) with a threshold corresponding to 10 % of the mean shear rate, we observe the presence of such low-drag events at $Wi = 8$. Note that the choice of threshold is arbitrary here and a definitive choice of the threshold value is absent in the literature. Effectively, for the considered viscoelastic turbulent flow at $Wi = 8$, we observe a drag reduction (quantified as $1 - (Re_\tau/Re_{\tau,Wi=0})^2$, see also Izbassarov *et al.* (2021)) of roughly 20 % for the set of considered parameters in this study. From figure 2, it is evident that the fields at the wall (which are provided as inputs to FCN, see figure 1, § 2.2) significantly deviate from the statistical mean for a considerable fraction of the total time. Thus, in this work, we aim to build a neural network model that can predict viscoelastic turbulence quantities of interest, not only in the mean flow, but also in extreme wall-shear events with particular interest in hibernation intervals.

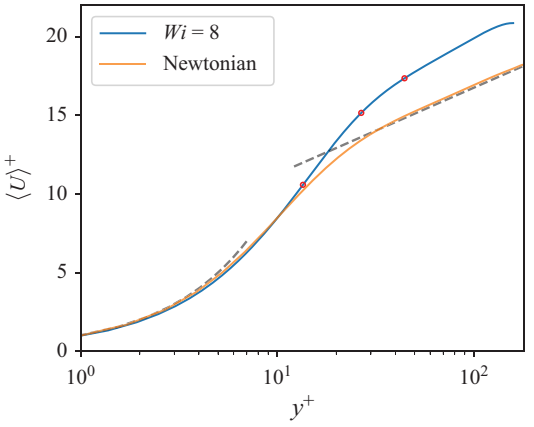

Figure 3. Inner-scaled mean streamwise velocity profile obtained with the viscoelastic channel flow at $Wi = 8$ (blue) and reference Newtonian channel flow (orange). The red markers indicate the wall-normal positions at which planar data are sampled, apart from the wall. The black dashed lines corresponds to the viscous sub-layer ($\langle U \rangle^+ = y^+$) and log-law ($\langle U \rangle^+ = \ln(y^+)/0.41 + 5.2$) relationship.

To this end, a database consisting of instantaneous fluctuation fields (obtained by the subtraction of mean value of viscoelastic turbulent fields) of wall-shear-stress components and wall-pressure fluctuation, as well as the two-dimensional velocity-fluctuation and polymeric-stress-fluctuation fields obtained at different wall-normal locations, $y^+ = 13.6$, 26.7 and 44.2 ($y/h \approx 0.09$, 0.17 and 0.28, respectively, see also figure 3) is generated. Note that these wall-normal locations correspond respectively to $y^+ = 15$, 30 and 50 for a Newtonian turbulent channel flow and, hence, for simplicity, we refer to these locations as $y^+ \approx 15$, 30 and 50, respectively, in this study. The buffer region is probed because of its importance in terms of production and dissipation of turbulent energy, and is significantly modified in drag-reducing flows with polymer additives (Den Toonder *et al.* 1997; Stone & Graham 2003).

The simulations are run for $\sim 120h/u_\tau$ time units and a total of 40 600 samples is obtained with a sampling period of $\Delta t_s^+ \approx 1$ for training the network model. The sampled instantaneous two-dimensional fields are down-sampled to a resolution of $(N_x \times N_z =)\ 432 \times 432$ in x and z, respectively. The fields on both walls are used in this study, and they are split into training and validation sets with a ratio of 4 : 1. The computational resources required to carry out the simulation and generate the necessary training dataset amounted to approximately 1.5 million core-hours.

The network models are evaluated with the samples in the test dataset which consists of 10 000 samples. The samples in the test dataset are chosen from a time interval (in the sampled time series) that corresponds to at least 60 flow-through times apart from the samples in the training dataset to ensure minimal auto-correlation between the samples in the training and test dataset. The temporal length for the number of samples considered in the test dataset corresponds to $\approx 50h/u_\tau$ time units, whereas a temporal averaging over 10–15 eddy-turnover times is sufficient to obtain good convergence of turbulence statistics (Li, Sureshkumar & Khomami 2006).

2.2. *Neural network model*

In this work, a fully convolutional neural network model similar to the one proposed by Guastoni *et al.* (2021) is used, with an increased number of hidden layers (see figure 1) to obtain a more complex combination of abstract turbulent features identified

by the kernels in the network. Here, we use an existing architecture, acknowledging that further enhancements could be achieved with newer architectures that require extensive datasets. Our focus is on proposing a methodology for viscoelastic stress predictions in turbulent flows aimed towards experimental applications and in establishing baseline performance using current convolutional architectures. The considered FCN consists of 30 hidden layers with total number of trainable parameters amounting to 985 105 (≈ 1 million parameters). The convolution operations are followed by batch normalisation and a rectified-linear-unit (ReLU) activation function. The inputs to the network are normalised using respective mean and standard deviation of the fields from the training dataset and the outputs are normalised using the corresponding standard deviation values. For the different prediction tasks considered in this study, the choice of loss function ($\mathcal{L}$) is the mean-squared error (MSE) between the instantaneous predicted and DNS fields:

$$\mathcal{L}(\boldsymbol{u}_{FCN}; \boldsymbol{u}_{DNS}) = \frac{1}{N_x N_z} \sum_{i=1}^{N_x} \sum_{j=1}^{N_z} |\boldsymbol{u}_{FCN}(i, j) - \boldsymbol{u}_{DNS}(i, j)|^2 , \tag{2.7}$$

which helps the network to learn the large-scale features first and then progressively optimse the trainable parameters to minimise the errors at finer scales (Xu *et al.* 2019). The subscripts 'DNS' and 'FCN' are respectively used to denote the DNS samples and corresponding predictions from FCN. Each network model is trained using $4 \times$ A100 graphics-processing units (GPUs), amounting to approximately 3500 GPU-hours for training a single network model.

In this study, three types of predictions have been undertaken to highlight the capability of FCN models to reconstruct the near-wall visco-elastic turbulence fields. In V-predictions (indicating velocity predictions), the streamwise wall-shear stress, spanwise wall-shear stress and pressure field at the wall are used to predict the streamwise, spanwise and wall-normal velocity fluctuations at the target wall-normal position. This allows us to assess whether velocity fields can also be predicted in viscoelastic turbulence exhibiting periods of hibernation. The performance of the neural network models in predicting the fluctuations of polymeric shear stress ($\tau_{p,\,\mathrm{xy}}$) and fluctuations of trace of polymeric stress ($\mathrm{tr}(\tau_p)$) at a given wall-normal location using the true velocity-fluctuation fields at the same location are denoted as E predictions (signifying prediction of elastic/polymeric stress quantities of interest). In this study, the fluctuations of polymeric-stress components are predicted directly from the input data. Finally, in V-E predictions, the FCN model is used to predict the fluctuations of polymeric shear stress and diagonal components of polymeric-stress tensor at a target wall-normal distance directly from wall inputs, with auxiliary predictions of corresponding velocity fluctuations at the considered wall-normal location. The auxiliary predictions of velocity fluctuations at a wall-normal location are used in V-E predictions to obtain an increase in the accuracy of the prediction of polymeric-stress quantities. It is worth noting that the mean of polymeric shear stress can be obtained either from the experimentally quantified stress deficit (Warholic *et al.* 1999) or from numerical simulations. Additionally, the FCN model performs well in predicting the mean of polymeric-stress quantities, which stems from the use of the mean-squared error as a loss function that tends to regress to the mean and hence the relative errors in predicting the mean polymeric-stress quantities from FCN are lower than 2 %. Consequently, our primary focus in this study is on retrieving the instantaneous fluctuations of polymeric stress using corresponding fluctuations of input quantities.

The mean absolute error between the predictions and DNS fields (denoted by MAE) is reported for different types of predictions, which is calculated as

$$\mathrm{MAE}(u) = \langle |u_{FCN} - u_{DNS}| \rangle_{x,z}. \tag{2.8}$$

The error metrics described in this section are computed for each component of $\boldsymbol{u}$ and for the polymeric-stress quantities of interest (refer to Appendix A). The network performance is also evaluated from a statistical point of view in terms of the relative error in predicting the corresponding r.m.s. quantities between the true (DNS) fields from the test dataset and the fields predicted by the FCN (indicated by E_{rms}), and is given by

$$E_{rms}(u)\ [\,\%] = 100 \cdot \frac{|u_{FCN,rms} - u_{DNS,rms}|}{u_{DNS,rms}}, \tag{2.9}$$

whereas the instantaneous correlation coefficient between the predicted and the DNS fields is defined as

$$R(u) = \frac{\langle u_{FCN} u_{DNS} \rangle_{x,z,t}}{u_{FCN,rms} u_{DNS,rms}}, \tag{2.10}$$

with $\langle \cdot \rangle_{x,z,t}$ corresponding to the average in space (x, z) and time (t; denotes the samples in the test dataset) and subscript $\cdot_{rms}$ refers to r.m.s. quantities.

Note that the performance metrics reported in this study are obtained from the mean of at least three different network models to include the effects of stochasticity introduced by the random initialisation of kernel weights in FCN and random sampling of mini-batches during the training process. The instantaneous correlation coefficient between the predicted and DNS fields averaged over the samples in the test dataset, is also highlighted. To evaluate the distribution of energy across the various scales in the flow, a comparison of the pre-multiplied two-dimensional (2-D) power-spectral density (PSD) $k_z k_x \phi_{ij}(\lambda_x^+, \lambda_z^+)$ between DNS fields and the predictions is performed. Here, ϕ_{ij} is the power-spectral density obtained for the quantity 'ij' and k_x, k_z respectively denoting the wavenumbers in streamwise and spanwise directions, with the corresponding wavelengths in viscous units denoted by λ_x^+ and λ_z^+.

2.3. *Low-pass filtering of velocity fluctuations*

To identify the effects of small-scale features in the input velocity-fluctuation fields on the predictions of polymeric stress (see §§ 3.5 and 3.6) and thereby to recommend scale requirements for inputs from possible experimental investigations, we employ low-pass filtering of velocity fluctuations with a threshold wavelength denoted by λ_c^+. This threshold λ_c^+ represents the smallest wavelength of the turbulent scales present in the input velocity-fluctuation fields to the FCN. For instance, in velocity-fluctuation fields sampled from DNS with 432×432 data points respectively in the streamwise and spanwise directions, the minimum wavelengths correspond to $\lambda_x^+ = 5$, $\lambda_z^+ = 2.5$ and hence, $\lambda_c^+ = 2.5$ for the DNS sampled fields. By filtering the sampled DNS velocity-fluctuation fields at a certain y^+ to contain small scales above λ_c^+, we ascertain that $\lambda_x^+ = \lambda_z^+ \geq \lambda_c^+ (> 2.5)$. However, the predictions of polymeric-stress quantities from the FCN aim to capture all the scales above 2.5 viscous-length units, regardless of the input λ_c^+. In other words, the sampled DNS polymeric-stress quantities serve as the true reference for the supervised training process of FCN for all the different network models with corresponding λ_c^+ of input velocity fluctuations.

The filtering is performed in the wavenumber space k_x, k_z and the corresponding procedure for the filtering process is outlined in Algorithm 1.

The relative decrease in the turbulent kinetic energy in the input velocity fluctuations sampled from DNS (denoted by $\mathcal{K}_{DNS}$) and after the filtering process (denoted by $\mathcal{K}_f$) for

Algorithm 1 Low-pass filtering of input velocity fields

Input: λ_c^+, 2D field sequence $\chi_i \in \{u_1, u_2, ...u_N, v_1, v_2, ...v_N, w_1, w_2, ...w_N\}$
Output: 2D filtered field sequence $\zeta_i \in \{\tilde{u}_1, \tilde{u}_2, ...\tilde{u}_N, \tilde{v}_1, \tilde{v}_2, ...\tilde{v}_N, \tilde{w}_1, \tilde{w}_2, ...\tilde{w}_N\}$
for $i \leftarrow 1$ **to** $3N$ **do**
  Compute 2D-FFT of χ_i: $\mathcal{U}(k_x, k_z) \leftarrow \mathrm{FFT}(\chi_i)$
  2D-Shift FFT: $\mathcal{U}_{\mathrm{shift}}(k_x, k_z) \leftarrow \mathrm{FFTshift}(\mathcal{U})$
  if $\sqrt{\left(\frac{2\pi}{k_x \ell^*}\right)^2 + \left(\frac{2\pi}{k_z \ell^*}\right)^2} < \lambda_c^+$ **then**
    $\mathcal{U}_{\mathrm{shift}}(k_x, k_z) \leftarrow 0$
  end
  Inverse 2D-shift FFT: $\widetilde{\mathcal{U}}(k_x, k_z) \leftarrow \mathrm{IFFTshift}(\mathcal{U}_{\mathrm{shift}})$
  Compute inverse 2D-FFT of $\widetilde{\mathcal{U}}$: $\zeta_i \leftarrow \mathrm{IFFT}(\widetilde{\mathcal{U}})$
end
return $\boldsymbol{\zeta}$

a given λ_c^+ is quantified as

$$\Delta\mathcal{K} = 100 \cdot \frac{\mathcal{K}_{DNS} - \mathcal{K}_f}{\mathcal{K}_{DNS}} \,[\,\%] = 100 \cdot \frac{\langle \boldsymbol{\chi}^2 \rangle - \langle \boldsymbol{\zeta}^2 \rangle}{\langle \boldsymbol{\chi}^2 \rangle} \,[\,\%], \tag{2.11}$$

where $\langle \cdot \rangle$ corresponds to the spatial and temporal averaging of data yielding a scalar output. Here, $\boldsymbol{\chi}$ corresponds to the sequence of sampled velocity-fluctuation snapshots from DNS and $\boldsymbol{\zeta}$ is the sequence of respective filtered fields obtained from the filtering process.

3. Results

The predictions of the trained network models are compared with the data obtained from DNS. The performance is assessed from a qualitative point of view and subsequently from a quantitative aspect, based on predictions of instantaneous fields, turbulent statistics and the two-dimensional power spectral density. Further, the importance of small-scale velocity fluctuations to successfully retrieve the small-scale polymeric-stress fluctuations is highlighted. Table 1 summarises the list of predictions considered in this study.

3.1. *Prediction of velocity fluctuations*

The predicted velocity fluctuations at different target wall-normal positions using streamwise and spanwise wall-shear rate and wall pressure are qualitatively inspected. A sample prediction of the instantaneous velocity-fluctuation fields for the case of V predictions is shown in figure 4 (corresponding to an instant in the test dataset where the input wall-shear rate is higher than the mean wall-shear rate). We note that the predicted velocity fields are visually well correlated with the DNS fields at different target wall-normal locations. The linear correlation coefficient between the predicted and true streamwise-velocity fluctuation fields exceeds 99 % for predictions at $y^+ \approx 15$, and gradually declines but remains above 80 % at $y^+ \approx 50$. The r.m.s. quantities of the streamwise velocity-fluctuation fields at $y^+ \approx 15$, 30, 50 are predicted with less than ($E_{rms} <$) 3 %, 6 % and 15 % error, respectively. With an increasing separation distance

Section	Inputs	Outputs	Input y^+	Output y^+	λ_c^+	Type
	u_y, w_y, p	u, v, w	0	15	–	
3.1	u_y, w_y, p	u, v, w	0	30	–	V predictions
	u_y, w_y, p	u, v, w	0	50	–	
	u, v, w	$\mathrm{tr}(\boldsymbol{\tau_p}), \tau_{p,\,\mathrm{xy}}$	15	15	–	
3.2	u, v, w	$\mathrm{tr}(\boldsymbol{\tau_p}), \tau_{p,\,\mathrm{xy}}$	30	30	–	E predictions
	u, v, w	$\mathrm{tr}(\boldsymbol{\tau_p}), \tau_{p,\,\mathrm{xy}}$	50	50	–	
	u_y, w_y, p	$\mathrm{tr}(\boldsymbol{\tau_p}), \tau_{p,\,\mathrm{xy}}$	0	15	–	
3.2	u_y, w_y, p	$\mathrm{tr}(\boldsymbol{\tau_p}), \tau_{p,\,\mathrm{xy}}$	0	30	–	V-E predictions
	u_y, w_y, p	$\mathrm{tr}(\boldsymbol{\tau_p}), \tau_{p,\,\mathrm{xy}}$	0	50	–	
	$\tilde{u}, \tilde{v}, \tilde{w}$	$\mathrm{tr}(\boldsymbol{\tau_p}), \tau_{p,\,\mathrm{xy}}$	15	15	9–108	
3.4	$\tilde{u}, \tilde{v}, \tilde{w}$	$\mathrm{tr}(\boldsymbol{\tau_p}), \tau_{p,\,\mathrm{xy}}$	30	30	9–108	Filt
	$\tilde{u}, \tilde{v}, \tilde{w}$	$\mathrm{tr}(\boldsymbol{\tau_p}), \tau_{p,\,\mathrm{xy}}$	50	50	9–108	

Table 1. Summary of the predictions obtained using respective FCN models.

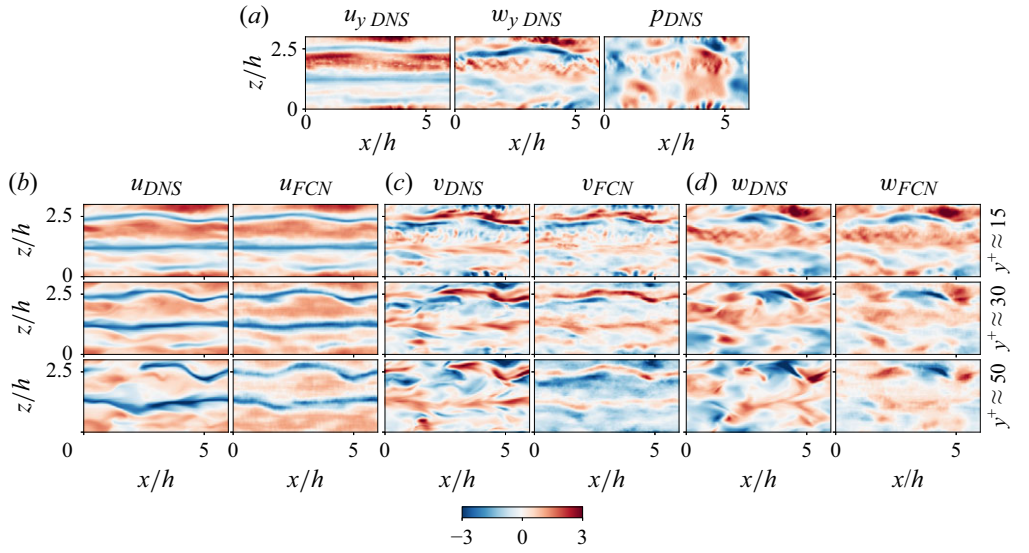

Figure 4. Sample instantaneous (*a*) normalised wall inputs to the FCN compared with the instantaneous velocity-fluctuation fields in the (*b*) streamwise, (*c*) wall-normal and (*d*) spanwise directions, at different wall-normal positions. In panel (*b*–*d*): (left) DNS field and (right) V predictions from FCN. The fields are scaled with the corresponding r.m.s. values.

(wall-normal distance between the wall fields and the target velocity-fluctuation fields), the fields are less correlated and thereby the performance of the network also decreases. Because of this, the r.m.s.-normalised mean-absolute errors in the predicted streamwise-velocity fluctuations are 0.14, 0.29 and 0.47 at $y^+ \approx 15, 30, 50$, respectively (see also figure 5). The performance metrics for different network models, along with the error fields (representing the difference between reference DNS and the predictions) corresponding to the instantaneous field as illustrated in figure 4, are summarised in Appendix A.

The MAE in the wall-normal and spanwise fluctuation fields remained below 0.025 in the different target wall-normal locations considered in the study (refer to figure 5 for normalised quantities). However, the E_{rms} values in the wall-normal and spanwise-velocity

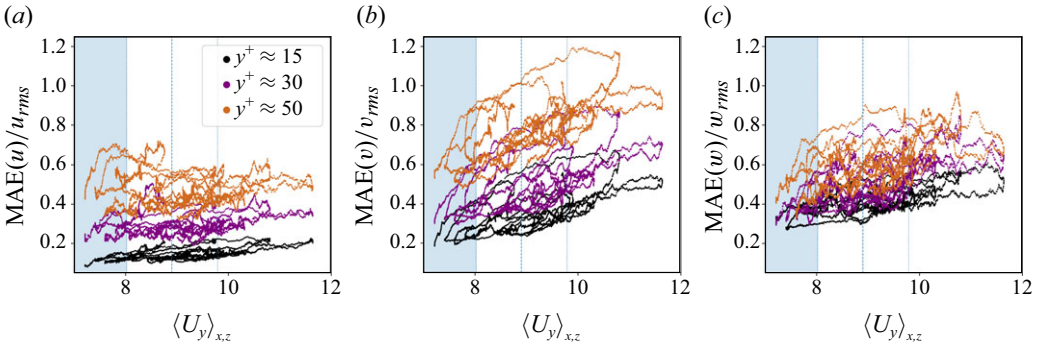

Figure 5. Variation of the r.m.s.-normalised mean-absolute errors of (*a*) streamwise, (*b*) wall-normal and (*c*) spanwise velocity components in V predictions at different wall-normal locations with respect to the wall-shear rate. The markers correspond to the mean absolute error in the instantaneous sample for the test dataset. The shaded region corresponds to the hibernation interval identified with 90 % of $\langle U_y \rangle_{x,z,t}$. The dashed vertical lines indicate the temporal mean and the dotted vertical lines indicate the 10 % deviation from the temporal mean.

fluctuations are at least twice as large as those obtained in the r.m.s. prediction of the streamwise component at the respective wall-normal locations. The reduction in accuracy stems from the weaker and finer-scale nature of wall-normal and spanwise fluctuations compared with the dominant streamwise component (see also figure 8*a*). Note that the polymers attenuate the spanwise and wall-normal fluctuations by opposing the upwash and downwash flows generated by near-wall vortices (Dubief *et al.* 2004, 2005). Thus, the absence of such polymeric stress information in the inputs for V predictions also limits the model's ability to accurately represent turbulence statistics in the spanwise and wall-normal fluctuation components. The reduced accuracy in predicting wall-normal and spanwise velocity fluctuations arises from their weaker and finer-scale nature compared with the streamwise component, further attenuated by polymer effects, making them harder for the model to learn without additional polymeric stress information.

It should be emphasised that the network model is explicitly optimised for predicting instantaneous fields rather than reproducing the turbulence statistics. This emphasis is rooted in the motivation for non-intrusive sensing in an experimental setting, aimed at understanding the near-wall dynamics of viscoelastic turbulent channel flow. In addition, optimising network models to accurately replicate turbulence statistics obtained from DNS could lead the model to learn the mean-flow behaviour with a lower E_{rms}. This may also entail a compromise, as predictions during hibernating intervals could potentially become less accurate.

When assessing the accuracy of the instantaneous predictions based on mean-absolute errors, as illustrated in figure 5, it becomes apparent that the MAE (in each test sample) varies with wall-shear rate for different target wall-normal locations. Specifically, in instances of low-wall-shear rate, the absolute errors are notably lower and increase with wall-shear rate. This is due to the fact that low-drag events typically exhibit reduced fluctuation intensity, which increases with wall-shear rate, leading to increased concentration of energy in small-scale features. Consequently, the network encounters relative difficulty in accurately predicting these small-scale features, resulting in higher prediction errors at large wall-shear-rate inputs. It is worth noting that the variation of MAE (in each test sample) with wall-shear rate stems from the selection of the loss function used in the network. Nevertheless, the obtained network model exhibits superior predictive performance in capturing velocity-fluctuation fields during low-wall-shear-rate

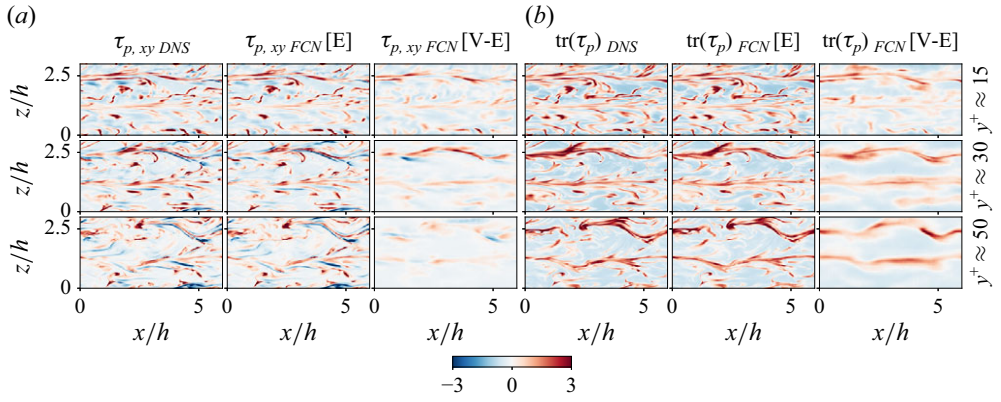

Figure 6. A sample fluctuation field corresponding to (*a*) polymeric shear stress and (*b*) trace of the polymeric stress, at different-wall normal locations. In panel (*a,b*): (left) the DNS field; (middle) E predictions; and (right) V-E predictions from FCN. The fields are scaled with the respective r.m.s. values.

events. This observation underscores the potential utility of such models in obtaining sufficiently accurate velocity fluctuations in an experimental setting, more particularly for studying hibernation events in detail.

3.2. *Prediction of polymeric stress*

The predicted velocity fluctuations at various target wall-normal positions show a good agreement with the reference DNS quantities. Following this, the focus is to estimate the polymeric-stress quantities of interest based on velocity fluctuations. Additionally, an effort is made to retrieve polymeric stress using only wall information, which is advantageous in experimental settings. This section begins with a qualitative analysis of the predicted polymeric-stress fields. A sample predicted field of polymeric-stress components (corresponding to the same time instant as the wall inputs shown in figure 4*a*) for E predictions and V-E predictions is shown in figure 6 (see also Appendix A, for the corresponding error fields). Overall, the large-scale features in the polymeric-stress quantities of interest are visually in good agreement with DNS. For E predictions, where polymeric stresses are predicted from DNS velocity fields at the same location, there is no separation distance between the input and target fields and the linear correlation coefficient between the predicted and DNS polymeric shear stress, and the trace of the polymeric stress remained more than 90 % for the different target wall-normal positions. Moreover, E_{rms} remained below 15 % for E predictions of $\tau_{p,xy}$ and tr(τ_p) at different target wall-normal distances.

Note that in V-E predictions, the polymeric stresses are predicted directly from the wall inputs, without having access to the true velocity fields at the wall-normal location where those stresses are predicted. Instead, predicted auxiliary velocity fields at that location (together with wall inputs) are used to predict the polymeric-stress fields. The obtained errors of approximately 40 % indicate that a small error in predicting velocity-fluctuation fields significantly impacts the errors in predicting the polymeric-stress fields (see also § 3.4), suggesting that the auxiliary velocity-fluctuation fields in V-E predictions lack certain information that is connected to the polymeric activity at the small wavelengths. Nevertheless, the large-scale structures in the predicted polymeric-stress fields for V-E predictions exhibit a qualitative agreement with the reference, as observed in figure 6.

Examining the accuracy of the instantaneous predictions based on mean-absolute errors, as depicted in figure 7 for E predictions and V-E predictions, reveals a similar trend in

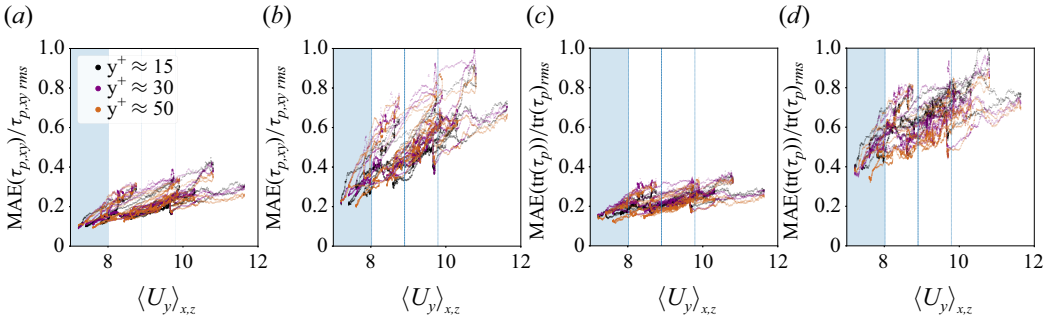

Figure 7. Variation of the r.m.s.-normalised mean-absolute errors of polymeric shear stress in (*a*) E predictions, (*b*) V-E predictions, and trace of polymeric stress in (*c*) E predictions and (*d*) V-E predictions with respect to the wall-shear rate. The markers correspond to the mean absolute error in the instantaneous sample in the test dataset. Shaded regions correspond to the identified hibernation interval with 90 % of $\langle U_y \rangle_{x,z,t}$. The dashed vertical lines indicate the temporal mean and the dotted vertical lines indicate the 10 % deviation from the temporal mean.

MAE (in each test sample) with respect to wall-shear rate as observed in V predictions. Overall, the absolute errors increase with the wall-shear rate. Further, the magnitude of such absolute errors in the field is nearly doubled for V-E predictions (figure 7*b*,*d*) compared with E predictions (figure 7*a*,*c*). Moreover, the MAE in predicting polymeric-stress quantities of interest remains relatively constant across various target wall-normal positions with respect to the corresponding r.m.s. quantities for E predictions and with marginal distinctions in V-E predictions.

3.3. *Energy distribution across different length scales*

The statistical analysis of the predicted velocity fluctuations using V predictions and the predicted polymer stresses using E predictions closely matches the results obtained from DNS. However, there is a significant deviation in the second-order statistics of polymeric stress quantities predicted using only the wall-shear rate and wall pressure (V-E predictions). To understand the reasons behind this, the distribution of energy across different length scales in the FCN predictions is examined and compared with the reference DNS.

The distribution of energy in the predicted and DNS data across different scales are compared through spectral analysis as illustrated in figure 8(*a*). The results show that the neural network models successfully reproduce the energy content in the streamwise velocity component (denoted by ϕ_{uu}) at different wavelengths. However, for the wall-normal velocity fluctuations (ϕ_{vv}) and spanwise velocity fluctuations (ϕ_{ww}), the network models exhibit limitations in reconstructing energy at the smallest wavelengths and specifically such errors in the smallest scales increase with increasing target wall-normal position.

The power spectral density obtained for the polymeric shear stress (denoted by $\phi_{\tau_{p,xy}\tau_{p,xy}}$) and the trace of polymeric stress ($\phi_{\mathrm{tr}(\tau_p)\mathrm{tr}(\tau_p)}$) are depicted in figure 8(*b*) for different wall-normal positions. We observe that the energetic structures correspond to wavelengths that are almost one order of magnitude smaller than those observed in the velocity fluctuations (refer to figure 8*a*). This reveals that the polymer activity is predominantly concentrated in small-scale structures compared with the flow scales. Consequently, this suggests that the employed neural network model needs to reconstruct fine-scale polymeric-stress fields from coarse energy-containing features in the velocity fluctuations.

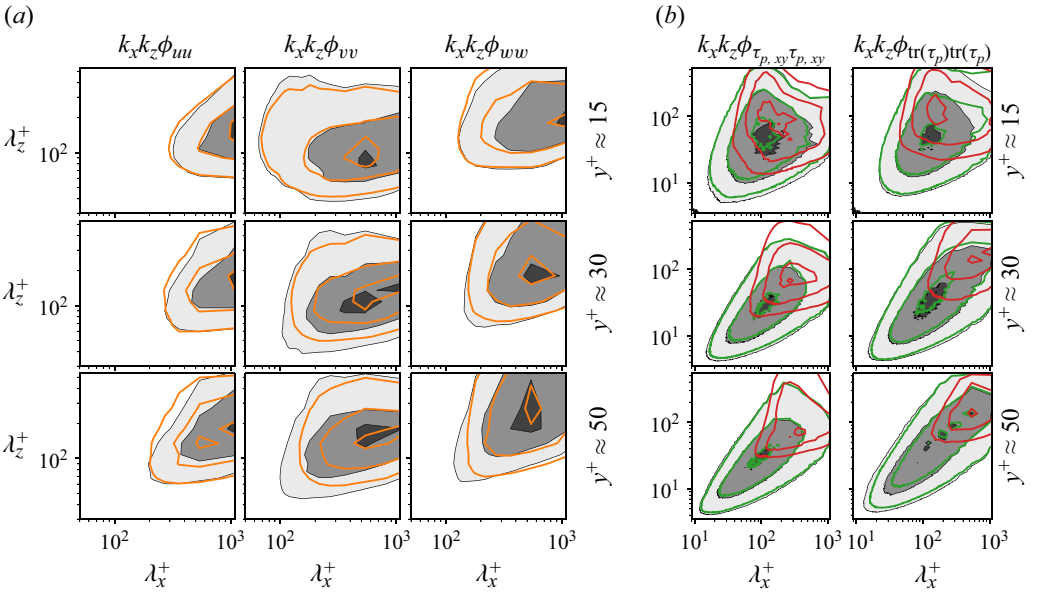

Figure 8. Pre-multiplied two-dimensional power-spectral densities of (*a*, left) the streamwise, (*a*, centre) wall-normal, (*a*, right) spanwise velocity components and (*b*, left) polymeric shear stress, (*b*, right) trace of polymeric stress at $y^+ \approx 15$ (top), $y^+ \approx 30$ (middle) and $y^+ \approx 50$ (bottom). The contour levels contain 10 %, 50 % and 80 % of the maximum power-spectral density. Shaded contours refer to DNS data, while contour lines correspond to (*a*) V predictions, (*b*, green) E predictions and (*b*, red) V-E predictions.

For the E predictions (figure 8*b*), where exact velocity fields from DNS at the same wall-normal position are used as inputs, we observe the ability of the model to reconstruct the features containing energy at different wavelengths more accurately with minimal errors observed in the smallest scales. However, in the case of V-E predictions, where the wall inputs to the network feature large-scale energy-containing features, the performance of the network is reduced in reconstructing the energy distribution of features at smaller scales, and rather the model tends to predict the large-scale features in the polymeric-stress fields. These observations underscore the importance of providing accurate velocity-fluctuation fields as inputs to the FCN. Although the auxiliary velocity fields have a very small error compared with DNS velocity fields, they lack certain information when reconstructed by FCN using wall inputs in V-E predictions, and thereby the network is unable to capture the polymeric-stress features at small and medium scales.

3.4. *Effects of small-scale velocity fluctuations on the polymeric stress predictions*

Spectral analysis reveals that the energetic scales in velocity fluctuations are approximately one order of magnitude larger than those in the polymeric-stress quantities of interest. Consequently, it becomes challenging for the FCN to reconstruct polymeric stress information at finer scales using the large energy-containing structures in velocity fluctuations. Furthermore, for E predictions, DNS velocity fluctuation fields are used as inputs whereas for V-E predictions, the (auxiliary) inputs are the predicted velocity fluctuations at a target wall-normal position that exhibits a good agreement with the DNS velocity-fluctuation fields. It should be highlighted that the (auxiliary) velocity-fluctuation fields employed in V-E predictions quite accurately comprise the large-scale features as observed with DNS fields, although they exhibit certain differences in the small-energy

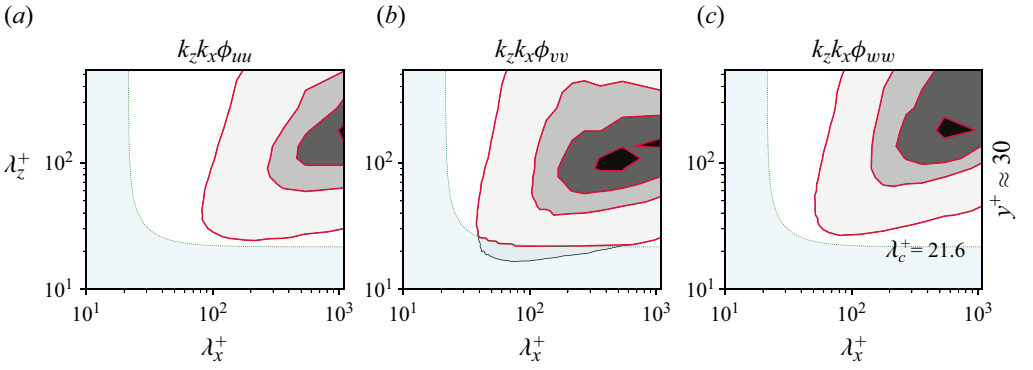

Figure 9. Pre-multiplied two-dimensional power spectral density of (*a*) streamwise, (*b*) wall-normal and (*c*) spanwise velocity fluctuations at $y^+ \approx 30$. The contour levels contain 10 %, 50 %, 80 %, 99 % of the maximum power spectral density. Shaded contours in grey refer to DNS data, while contour lines in red indicate the corresponding energy levels after filtering with $\lambda_c^+ = 21.6$. Filtered scales are indicated by the shaded region in blue.

containing features (see also figure 8*a*). However, we observe that small-scale polymeric-stress fluctuations in V-E predictions are under-predicted compared with E predictions (see figure 6). This indicates that small-scale velocity fluctuations in DNS fields are crucial for the accurate prediction of polymeric stresses. Thereby, the observations also signify that polymeric stresses and velocity fluctuations are strongly coupled at fine, low-energetic scales.

We investigate the relationship between polymeric stress and velocity fluctuations at smaller scales by systematically removing the turbulent kinetic energy at these finer scales and observing the resulting polymeric stress predictions by FCN. The low-pass filtering of velocity fluctuations (as outlined in § 2.3) is performed to evaluate the accuracy of prediction of polymeric stresses by using only the large energy-containing features in velocity fluctuations. This approach not only helps in identifying the effects of small-scale features in the input velocity-fluctuation fields on the prediction of polymeric stress, but also enables a scale requirement recommendation for velocity fluctuations from potential experimental investigations to estimate the polymeric stress information. The effect of filtering velocity fluctuations using the pre-multiplied two-dimensional (2-D) power spectral density (PSD) $k_z k_x \phi_{kk}(\lambda_x^+, \lambda_z^+)$ for the velocity fluctuations ($k \in \{u, v, w\}$) at $y^+ \approx 30$ is shown in figure 9. The figure illustrates the effect of filtering the small-scale velocity fluctuations with a wavelength threshold of $\lambda_c^+ = 21.6$.

A sample instantaneous field of the trace of polymeric stress in the test dataset is shown in figure 10. The reference DNS field at different wall-normal locations is shown alongside the corresponding predictions obtained from FCN, with respective inputs at different cutoff wavelengths. It is observed that E predictions ($\lambda_c^+ = 2.5$) successfully capture all the different scales present in the reference DNS. As the cutoff wavelength in the input velocity fluctuations to FCN increases, the predicted outputs begin to lack certain small-scale features. At $\lambda_c^+ = 13.5$, where the absence of small scales contributes to a relative loss ($\Delta\mathcal{K}$) of less than 0.01 % of turbulent kinetic energy in the inputs at different y^+ considered here, the errors in the prediction of small scale become significant, as illustrated in figure 10. Further, for $\lambda_c^+ = 21.6$, constituting a relative loss of less than 0.07 % of TKE of inputs at different y^+ considered here, we observe that the small-scale features are increasingly depleted in the predictions. Nevertheless, the predictions still manage

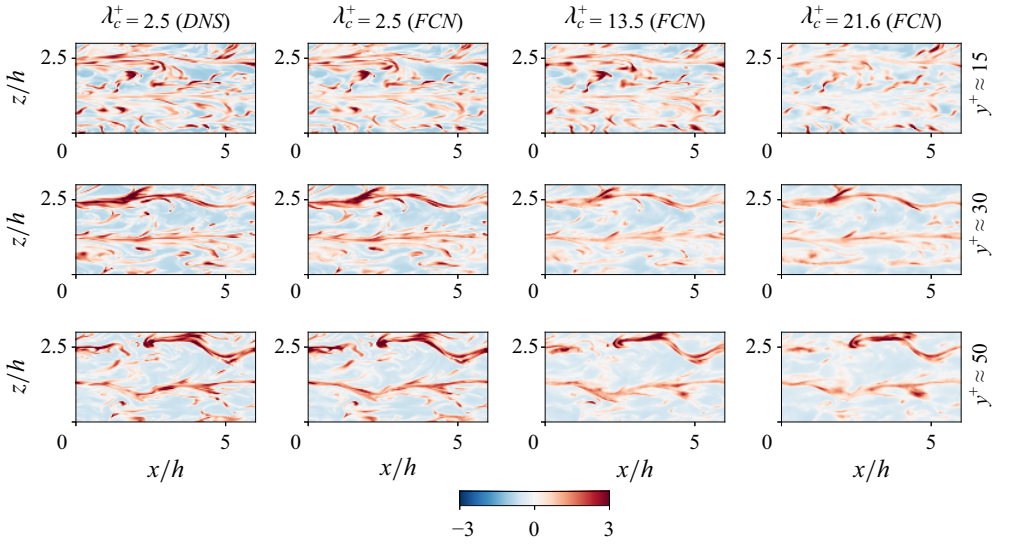

Figure 10. A sample trace of the polymeric-stress-fluctuation field is plotted at different wall-normal locations with corresponding predictions from FCN using inputs with different cutoff wavelengths of the velocity-fluctuation fields. The fields are scaled with the respective r.m.s. values.

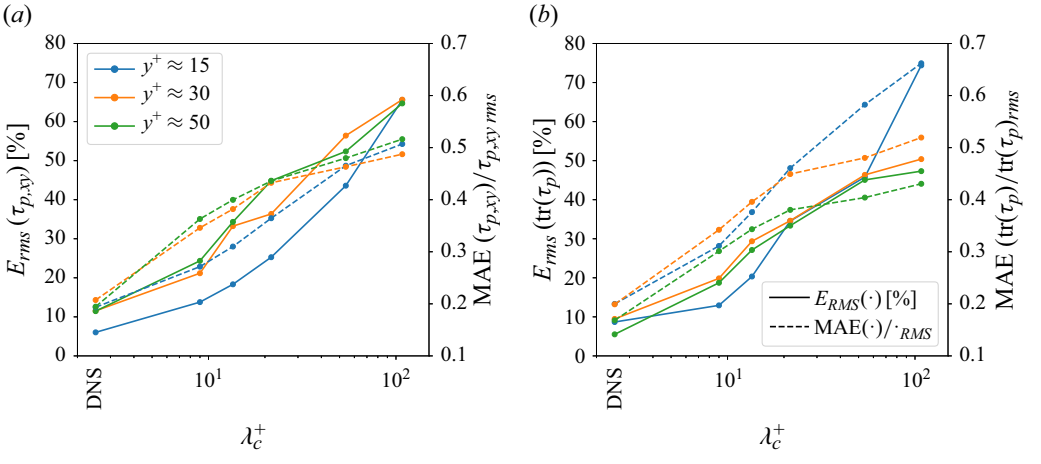

Figure 11. Variation of the errors in predicting r.m.s. fluctuations of (*a*) polymeric shear stress and (*b*) trace of polymeric stress with respect to the cutoff wavelength λ_c^+ of velocity-fluctuation fields at respective wall-normal locations. The cutoff wavelength for DNS simulations is $\lambda_c^+ = 2.5$ based on the spanwise resolution. The corresponding normalised mean-absolute errors are also indicated.

to capture the regions with large polymer extension, where $\mathrm{tr}(\tau_p)$ is higher. A similar observation for the polymeric shear stress is provided in Appendix B.

Overall, the variation of errors in predicting the corresponding r.m.s. quantities of the polymeric stress quantities of interest is shown in figure 11 for different values of cutoff wavelengths of inputs. The corresponding normalised mean-absolute errors are also indicated. Overall, the mean errors observed at different target wall-normal locations exhibit a logarithmic growth with respect to the cutoff wavelength of the input velocity fluctuations. This also explains the observation of higher errors in V-E predictions when using wall inputs to predict polymeric stress quantities of interest at different

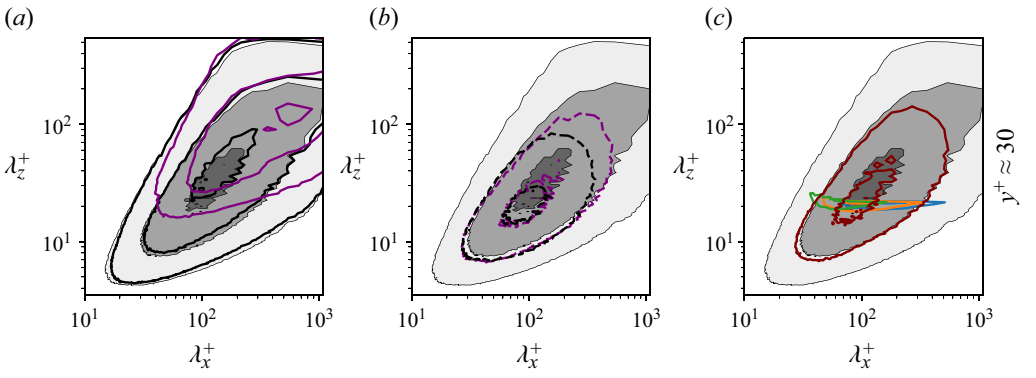

Figure 12. Pre-multiplied two-dimensional power spectral density of trace of polymeric stress at $y^+ \approx 30$. The shaded contours in all panels correspond to the spectra obtained from DNS samples $(\mathrm{tr}(\tau_p)_{DNS})$ in the test dataset. (*a*) Spectra when filtered and unfiltered velocity fields are used as inputs: DNS velocity-fluctuations is used as input $(\mathrm{tr}(\tau_p)_{FCN,DNS})$ (black), filtered velocity-fluctuations using a cut-off wavelength of $\lambda_c^+ = 21.6$ $(\mathrm{tr}(\tau_p)_{FCN,Filt})$ (purple). (*b*) Spectra of errors: the spectra of the difference between reference (DNS) and predicted polymeric-stress fluctuations using DNS velocity fluctuations as input $(\mathrm{tr}(\tau_p)_{DNS} - \mathrm{tr}(\tau_p)_{FCN,DNS})$ (black), filtered velocity fluctuations (with $\lambda_c^+ = 21.6$) as input $(\mathrm{tr}(\tau_p)_{DNS} - \mathrm{tr}(\tau_p)_{FCN,Filt})$ (purple). (*c*) Spectra of the difference between unfiltered and filtered cases: the spectra of the difference between reference DNS velocity fluctuations and the filtered velocity fluctuations with $\lambda_c^+ = 21.6$ for u, v, w components are indicated in blue, orange and green contour lines, respectively, while brown contour lines depict the spectra of the difference between the predicted polymeric-stress fluctuations with unfiltered and filtered inputs $(\mathrm{tr}(\tau_p)_{FCN,DNS} - \mathrm{tr}(\tau_p)_{FCN,Filt})$. The contour levels in all panels and contour lines in panel (*a*) contain 10 %, 50 % and 80 % of the maximum power spectral density, while contour lines in panel (*b*,*c*) indicate 10 % and 50 % of the respective maximum power spectral density.

y^+ compared with E predictions. Although the predicted velocity fluctuations from V predictions closely resemble those of the DNS reference, there is a logarithmic increase in prediction errors of polymeric stresses when using the auxiliary predictions of velocity fluctuations, which lacks energy content at certain scales (see figure 8*a*).

In addition, for retrieval of polymeric stress information from possible near-wall experimental velocity fields using FCN, it becomes necessary to resolve finer scales, typically lower than 10 viscous lengths, to obtain more reliable polymeric-stress behaviour at the smallest scales. This hypothesis will be confirmed more conclusively in the next section, where we further examine the effects of artificially excluding small scales from the DNS velocity fields.

3.5. *Spectral analysis on the effects of small-scale velocity fluctuations*

Identifying the influence of small-scale features in the velocity-fluctuation fields on the polymeric stress, we probe the distribution of energy in the predicted polymeric stresses due to the absence of small, low-energetic scales in the velocity fluctuations. The pre-multiplied two-dimensional PSD of the trace of polymeric stress $(\mathrm{tr}(\tau_p)$ at $y^+ \approx 30$ is depicted in figure 12. Figure 12(*a*) shows the 10 %, 50% and 80% contours of reference (DNS) polymeric stress by shaded contours, against the FCN predictions of the trace of polymeric stress using DNS velocity-fluctuation fields as input to FCN $(\mathrm{tr}(\tau_p)_{FCN,DNS})$ (black contour lines) and filtered velocity fluctuations as input to FCN $(\tau_p)_{FCN,Filt})$ (purple contour lines).

The predictions using exact velocity fields closely capture the energy content across different scales compared with the reference (DNS) polymeric stress (black contours are almost identical to shaded contours in figure 12*a*). However, it should be noted that there

are always some small errors in predicting the trace of polymeric-stress fields using DNS velocity fluctuations as input. These errors stem from the absence of certain correlations in the inputs, such as the wall-normal gradients of velocity fluctuations and the time history of velocity fluctuations.

However, filtering the input velocity fluctuations with $\lambda_c^+ = 21.6$, so that they lack the very finest scales, results in a very significant deviation in the power density spectra of the predicted polymeric stress (purple contours are very different from shaded contours). Most notably, the energy-containing structures in the predictions are at larger spatial scales than in the DNS. Additionally, the predictions now lack certain small-scale energy components. This shows that polymers interact with very small scales in the velocity fields in viscoelastic turbulence. The similarity between purple contours (predictions with filtered velocity fields) and red contours in figure 8(*b*) (V-E predictions) confirms that errors in V-E predictions stem from the absence of the smallest scales in the auxiliary velocity fields.

The difference between the FCN predictions and the DNS reference polymeric-stress field represents the error in the predictions. To analyse this error quantitatively, we show the error spectra in figure 12(*b*). The error spectra illustrate the difference between the reference and predicted polymeric-stress fluctuations using DNS velocity fluctuations as input ($\mathrm{tr}(\tau_p)_{DNS} - \mathrm{tr}(\tau_p)_{FCN,DNS}$, black dashed contour), and the difference between reference (DNS) and predicted polymeric-stress fluctuations, using filtered velocity fluctuations with a cutoff wavelength of $\lambda_c^+ = 21.6$ as input ($\mathrm{tr}(\tau_p)_{DNS} - \mathrm{tr}(\tau_p)_{FCN,Filt}$), is depicted by a purple dashed contour. From figure 12(*b*), we observe that the errors are highest at the small yet energetic scales of the trace of polymeric stress, while large scales are less affected by errors. This confirms the visual finding from figure 6 that the largest scales are relatively well captured by V-E predictions.

Finally, from figure 12(*c*), we examine the effect of filtering small scales in the velocity fluctuations on the differences introduced in the predictions by the FCN. Here, the spectra of the difference between the predicted polymeric-stress fluctuations with DNS inputs (refer to figure 12*a*, black contour lines) and the predicted polymeric-stress fluctuations (refer to figure 12*a*, purple contour lines) with filtered inputs ($\mathrm{tr}(\tau_p)_{FCN,DNS} - \mathrm{tr}(\tau_p)_{FCN,Filt}$) is plotted with brown contour lines. In addition, we include the spectra of the difference between reference DNS velocity fluctuations and filtered velocity fluctuations with $\lambda_c^+ = 21.6$ for u, v, w components (respectively indicated with blue, orange and green contour lines). The latter contours are very narrow, which shows that changes in velocity fields due to filtering mostly occur at a narrow range of scales. However, predictions of polymeric stresses are affected at a strikingly large range of scales (brown contours). Figure 12(*c*) hence shows that the loss of turbulent kinetic energy in the small scales in the velocity fluctuations does not necessarily correspond to the loss of energy at similar scales in the polymeric stress. This observation is aligned with the studies of Nguyen *et al.* (2016), where they showed from scale-to-scale analysis (Casciola & de Angelis 2007; Xi, Bodenschatz & Xu 2013; Valente, Da Silva & Pinho 2014) of isotropic viscoelastic turbulence that the loss of turbulent kinetic energy at a given small scale does not necessarily correspond to a gain of polymer energy at the same scale, and *vice versa*.

3.6. *Interpretation of predictions with filtered velocity fluctuations*

Overall, we observe that the small-scale features in the velocity-fluctuation fields are crucial for the estimation of polymeric stress. In this section, the reason for such an observation is hypothesised based on polymer–flow interaction and obtained predictions from FCN. We start with the observation of the probability distribution function of

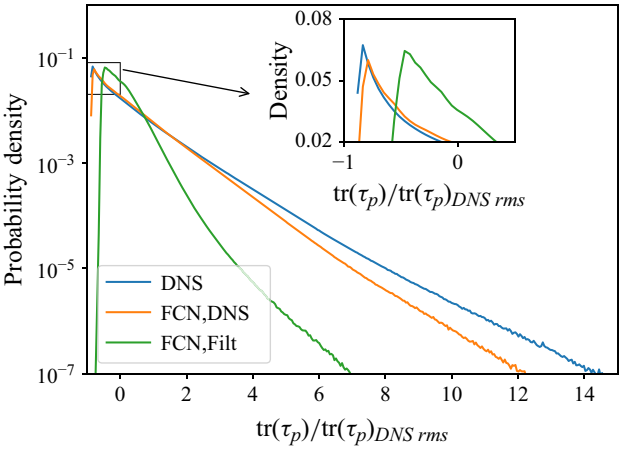

Figure 13. Probability density function of the r.m.s.-normalised trace of polymeric stress at $y^+ \approx 30$, identifying the distribution of the percentage of data-points in the test dataset with a bin size of 0.045. (Inset) Magnified view of the peak of distribution.

polymeric stress. The probability distribution function for the trace of polymeric stress is shown in figure 13. The predictions from FCN using DNS input velocity fluctuations closely capture the resulting probability distribution function observed with the DNS stress fields in the test dataset. However, using the filtered velocity-fluctuation fields with $\lambda_c^+ = 21.6$ results in the distribution of the data to be closer to the mean value. The negative and positive fluctuations of the trace of the polymeric stress are under-predicted indicating that the relaxation behaviour of the polymer is over-predicted and the maximum stretch of polymers is under-predicted by FCN. The over-prediction and under-prediction of polymeric stress may stem from the fact that the FCN is optimised to capture the mean behaviour of the polymeric-stress fluctuations for the given velocity-fluctuation input. Because of the alteration of the input velocity-fluctuation field via filtering of small scales, the FCN is unable to predict well the extreme behaviour of polymeric stress, and thereby converges close to the mean behaviour and hence the resulting prediction of the standard deviation of the polymeric stress quantities of interest are lower in comparison to that observed with the DNS fields. Consequently, this contributes to growing errors with respect to the cutoff wavelength of input velocity fluctuations. However, there may be physical reasons attributed to the difficulty in predicting polymeric stress without small-scale features in velocity fluctuations that are independent of the chosen technique to model the relationship between polymeric stress and velocity fluctuations. Future work will involve performing direct numerical simulations with filtered velocity fluctuations to identify the effects of small-scale velocity fluctuations on the polymeric-stress-fluctuation fields. Additional tasks also include transfer-learning-based approaches to evaluate the performance of the network models at different Weissenberg numbers.

Filtering small scales in the velocity-fluctuation fields results in an alteration of the turbulent kinetic energy of the flow. In the buffer region that is considered in the study, there exists an anti-correlation between streamwise velocity fluctuation and the fluctuations of the trace of polymeric stress (as shown in figure 14), thereby an increase in polymeric stresses (and consequently polymer energy) leads to a decrease in the turbulent kinetic energy of the fluid (see also figure 15*a*).

The r.m.s.-normalised joint probability distribution of the prediction errors in the trace of polymeric stress with respect to turbulent kinetic energy is probed in figure 15(*a*).

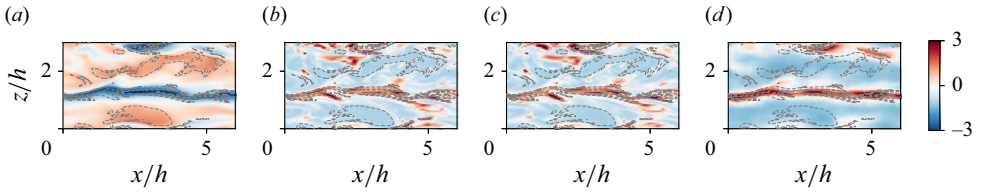

Figure 14. Instantaneous (a) streamwise velocity-fluctuation field and (b) trace of polymeric stress from the test dataset at $y^+ \approx 50$, alongside corresponding (c) E prediction and (d) V-E prediction. Contour lines indicate regions of strong anti-correlation between u and $\mathrm{tr}(\tau_p)$ as obtained with the DNS data.

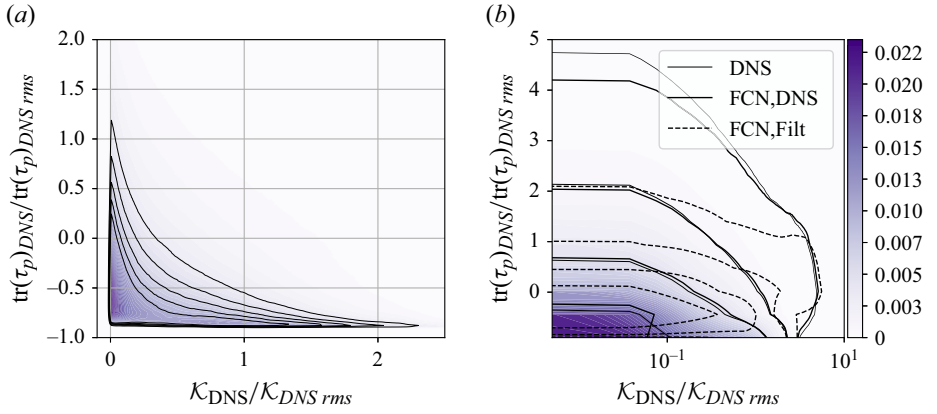

Figure 15. Normalised joint probability density function between turbulent kinetic energy and the trace of polymeric stress at $y^+ \approx 30$, obtained from (a) DNS samples in test dataset and (b) FCN predictions using DNS velocity fluctuations (FCN,DNS) and filtered velocity fluctuations (FCN,Filt) at $\lambda_c^+ = 21.6$.

From the figure, the relationship between the trace of polymeric stress (indicative of polymer stretch and elastic energy stored by polymers) and the turbulent kinetic energy of the flow from DNS samples in the test dataset is observed. It is evident that the polymers are highly stretched in regions with low turbulent kinetic energy and *vice versa*. This suggests that polymers extract turbulent kinetic energy from the fluid, particularly in the considered wall-normal position in the buffer region. Moreover, the relaxation of the polymeric stress, which can occur in the core of the streamwise vortices, releases energy into the fluid flow (Xi 2019).

From figure 15(b), it is observed that the under-prediction of the trace of polymeric-stress fluctuations is significant in the regions of lower turbulent kinetic energy. This indicates that the effect of filtering small scales results in over-prediction of relaxation behaviour of polymeric stress and under-prediction of maximum polymer elongation, and thereby maximum trace of polymeric stress, particularly in the regions with lower turbulent kinetic energy. Thus, due to the alteration of the distribution of small-scale input velocity fluctuations, the FCN model is unable to reproduce the features of energy extraction by polymers from the turbulent flow. Hence, it is pertinent to capture accurately the turbulent kinetic energy in the flow and that small-scale velocity fluctuations are required to accurately capture the extraction of turbulent kinetic energy from flow by polymers.

The results from the present study suggest that polymeric stress can be estimated by directly providing potential experimental measurements of wall quantities

(V-E predictions) or near-wall velocity fluctuations (E predictions) as inputs to the network model. It is important to note that experimental fields may contain noise, necessitating retraining of the network model using transfer learning methodologies to optimise the model weights with the acquired experimental dataset. However, in the current supervised learning framework, such approaches require the presence of reference experimental stress fields for retraining the network models, which is not applicable in this case. It was recently shown that Lagrangian stretching fields extracted from particle image velocimetry (PIV) serve as indicators of polymer elongation fields under certain conditions (Kumar, Guasto & Ardekani 2023), but their applicability to stress field substitutes in channel flow turbulence remains to be investigated. Therefore, we propose that as an initial step to gain insight into polymeric stresses from experimental measurements, interpolation (for matching resolution) and de-noising techniques (Raiola, Discetti & Ianiro 2015; Nekkanti & Schmidt 2021; Yousif *et al.* 2023*c*) can be employed to retrieve accurate wall fields or velocity fluctuations from experimental data. These refined velocity inputs can then be coupled with the proposed DNS-trained network models to obtain predictions of instantaneous polymeric-stress fields within the probed domain.

The present work can also be extended towards identifying coherent structures in the flow and thereby employing the SHapley Additive exPlanations (SHAP) algorithm to explain the importance of the coherent structure (Cremades *et al.* 2024), which can improve the understanding of the dynamical role of coherent structures in viscoelastic turbulent flow. Hence, the present work serves as a starting point, holding potential for many future works to understand better the polymer physics in drag-reduced flows.

4. Conclusions

The present work highlights the capability of a data-driven approach to perform non-intrusive sensing in viscoelastic turbulent flows. Here, we demonstrate the ability of CNN-based models to accurately reconstruct the velocity fluctuations in viscoelastic turbulence close to the wall, using the two wall-shear fluctuation components and the wall-pressure fluctuations as inputs. Additionally, the network models successfully reproduce the polymeric-stress-fluctuation fields from the DNS velocity-fluctuation fields. Moreover, the feasibility of these network models to extract polymeric-stress-fluctuation fields of interest solely from wall input fluctuations and predicted velocity fluctuations is explored. Overall, the network effectively reconstructs the large-scale features of the polymeric-stress fields using wall inputs and predicted velocity fields. Furthermore, the developed models exhibit enhanced accuracy in predicting quantities of interest during the hibernation intervals, facilitating a deeper understanding of the underlying physics during low-drag events when the model is deployed in a practical application. These non-intrusive-sensing models hold valuable applications in experimental settings (Vinuesa *et al.* 2023), enabling the determination of polymeric stresses in turbulent flows from velocity fields or wall inputs, which otherwise would be challenging or impossible to quantify experimentally. However, accurately predicting the polymeric stresses from wall inputs is found to be more challenging than predicting velocity fields from the same, since wall inputs typically do not contain fingerprints of the smallest scales, and we show that small scales in velocity fields are connected to a wide range of scales in polymeric-stress fields.

Aimed towards extracting polymeric-stress information from velocity-fluctuation fields in a possible experimental investigation of viscoelastic turbulent channel flow, a number of FCN models are trained with inputs corresponding to different thresholds of small-scale wavelengths in the velocity-fluctuation fields. We find that accurately capturing

the turbulent kinetic energy in the near-wall fields is crucial for retrieving second-order turbulent statistics of polymeric stresses. Specifically, experimental acquisition of velocity fluctuations would in principle need to resolve the finer scales, smaller than 10 viscous units, to obtain more reliable polymeric stress behaviour at the smallest scales, which determines the accurate rate of energy transfer from flow to polymers. We show that this in turn facilitates an accurate estimation of the r.m.s. of polymeric stresses in the buffer region of viscoelastic turbulent channel flow.

Concluding, the results demonstrate the potential of data-driven models to predict instantaneous fields in non-Newtonian wall turbulence, which is useful for flow control or estimation of stress fluctuations that cannot be measured. As a next step, de-noised experimentally measured velocity fields and wall pressure measurements could be given as inputs to the network that has been trained by simulations. Furthermore, direct numerical simulations with filtered velocity fluctuations can be performed to further isolate the physical mechanisms behind how small-scale velocity fluctuations influence the polymeric-stress-fluctuation fields at a wide range of scales.

Acknowledgements. The authors acknowledge the National Academic Infrastructure for Supercomputing in Sweden (NAISS) for providing the computational resources to carry out the numerical simulations and training of convolutional network models.

Funding. This work is supported by the funding provided by the European Research Council grant no. '2019-StG-852529, MUCUS' and the Swedish Research Council through grant No 2021-04820. R.V. acknowledges the ERC grant no. '2021-CoG-101043998, DEEPCONTROL'.

Declaration of interests. The authors report no conflict of interest.

Data availability statement. The data that support the findings of this study will be openly available on GitHub – KTH-Complex-fluids-group/2025_Prediction-of-flow-and-polymeric-stresses-in-a-viscoelastic-turbulent-channel-flow-using-FCN .

Appendix A. Performance metrics for network models

In the present study, hyperparameter tuning was conducted to investigate the sensitivity of various parameters, including network model capacity, depth, kernel size, batch size and learning rate, on the errors in predicting the r.m.s. of velocity and polymeric-stress fluctuations. Approximately 15 different training runs were performed to optimise these parameters, and a more thorough exploration of the hyperparameter space could further enhance prediction performance. In the present study, a fully convolutional neural network containing 3×3 kernels and 31 hidden layers constituting 985 105 trainable parameters is employed (refer figure 1). The initial weights for the network are distributed randomly with a Gaussian distribution and a scheduled learning rate (α) was provided to the Adam algorithm (Kingma & Ba 2015) in the form $\alpha = \alpha_0 a^{epoch/b}$, with α_0 corresponding to initial learning rate, and a, b are the tunable parameters denoted by learning rate drop and epoch drop, respectively (here, epoch corresponds to one entire pass of training data). In this study, $\alpha_0 = 0.001$, $a = 0.5$ and $b = 40$, and a batch size of 16 was employed in the training of FCN.

Additionally, U-Net (with five skip connections) and Generative Adversarial Network (GAN) models (with approximately 2 million trainable parameters in the generator) were also trained, and corresponding evaluations revealed comparable performance in terms of accuracy to that achieved with the FCN in the present study. Hence, the FCN with the optimal training parameters as obtained with the exploratory study is employed in the present work.

Parameters	y^+	i		
		u	v	w
$\langle \mathrm{MAE}(i) \rangle_t / i_{DNS\,rms}$	15	0.14 (± 0.01)	0.32 (± 0.11)	0.41 (± 0.02)
	30	0.29 (± 0.01)	0.44 (± 0.06)	0.53 (± 0.02)
	50	0.47 (± 0.01)	0.79 (± 0.15)	0.59 (± 0.04)
$E_{rms}(i)$	15	2.62 (± 1.2)	13.11 (± 2.7)	8.02 (± 3.8)
	30	5.21 (± 0.3)	15.90 (± 4.5)	10.62 (± 1.9)
	50	12.73 (± 3.9)	24.72 (± 6.5)	14.72 (± 4.4)
$R(i)$	15	0.996 (± 0.003)	0.889 (± 0.040)	0.932 (± 0.018)
	30	0.942 (± 0.002)	0.763 (± 0.015)	0.771 (± 0.010)
	50	0.811 (± 0.001)	0.623 (± 0.011)	0.643 (± 0.010)

Table 2. Model-averaged errors in V predictions.

Parameters	y^+	i			
		$\tau_{p\,\mathrm{xy}}\,[E]$	$\mathrm{tr}(\tau_p)\,[E]$	$\tau_{p\,\mathrm{xy}}\,[V-E]$	$\mathrm{tr}(\tau_p)\,[V-E]$
$\langle \mathrm{MAE}(i) \rangle_t / i_{DNS\,rms}$	15	0.19 (± 0.01)	0.20 (± 0.01)	0.45 (± 0.01)	0.63 (± 0.01)
	30	0.21 (± 0.01)	0.20 (± 0.02)	0.49 (± 0.02)	0.60 (± 0.01)
	50	0.19 (± 0.01)	0.17 (± 0.02)	0.48 (± 0.01)	0.55 (± 0.01)
$E_{rms}(i)$	15	6.03 (± 1.8)	8.68 (± 1.4)	42.52 (± 1.0)	54.71 (± 2.6)
	30	11.54 (± 2.7)	9.47 (± 1.8)	49.40 (± 3.4)	51.14 (± 0.7)
	50	11.46 (± 1.4)	5.52 (± 1.4)	62.37 (± 3.2)	49.54 (± 4.8)
$R(i)$	15	0.906 (± 0.004)	0.924 (± 0.007)	0.484 (± 0.006)	0.362 (± 0.013)
	30	0.906 (± 0.006)	0.917 (± 0.010)	0.296 (± 0.013)	0.433 (± 0.008)
	50	0.905 (± 0.007)	0.924 (± 0.011)	0.207 (± 0.012)	0.426 (± 0.015)

Table 3. Model-averaged errors in E predictions and V-E predictions.

The prediction errors for V predictions are provided in table 2 and various metrics for E predictions and V-E predictions are detailed in table 3. The error metrics reported in tables 2 and 3 are obtained from the samples contained in the test dataset and averaged over three different training runs for the FCN model. The variances are indicated in the braces.

The magnitude of point-wise errors in V predictions can go up to 1.2 for the wall-normal component as observed from figure 5(*b*) and the average value of $\langle \mathrm{MAE}(v) \rangle_t / v_{DNS\,RMS}$ at $y^+ = 50$ is 0.79, as indicated in table 2. While we acknowledge the presence of point-wise errors, quantified as $\langle \mathrm{MAE}(v) \rangle_t / v_{DNS\,RMS} \approx 1$ for larger target wall-normal positions, it is important to emphasise that the model effectively captures the dominant features in the fields, as evidenced by the spectra plots in figure 8(*a*). The spectral comparison indicates that the energy distribution across scales aligns well between the predicted and reference fields, highlighting the model's strength in reproducing the energy-containing structures. Additionally, the high correlation between the reference and predicted fields closer to the wall-parallel planes supports the conclusion that the model is successfully identifying and predicting the large-scale coherent features, such as streaks, in the turbulent flow. Thus, the overall ability of the model to reproduce the energy-containing structures closer to the

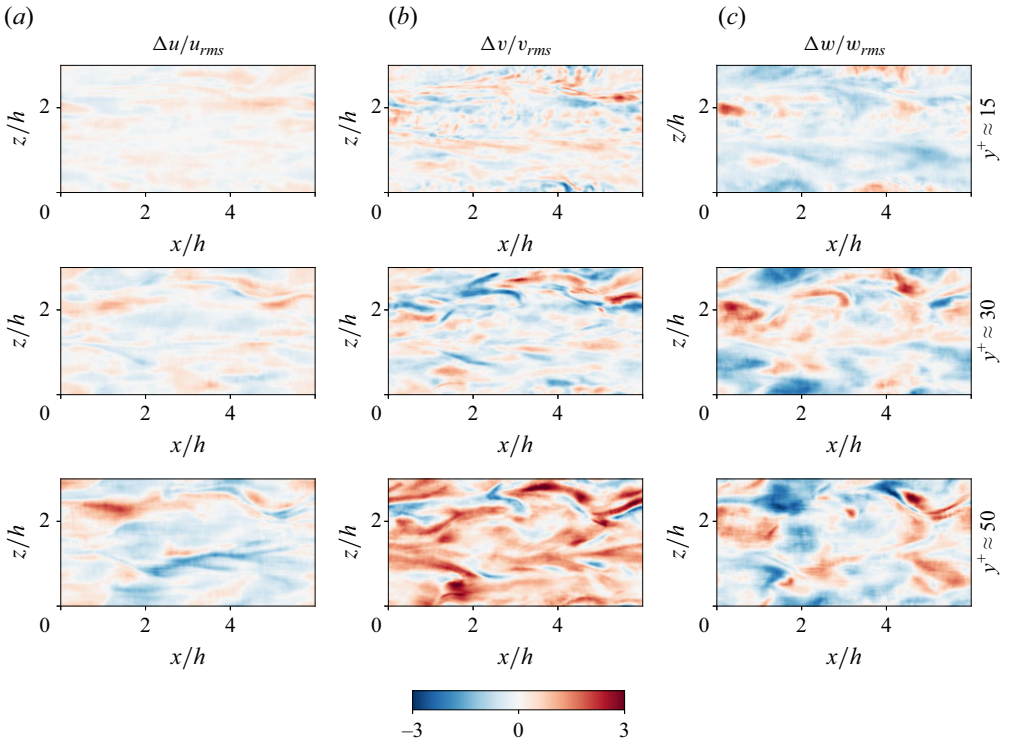

Figure 16. Error fields corresponding to V predictions of (*a*) streamwise, (*b*) wall-normal and (*c*) spanwise velocity fluctuations at different target wall-normal positions, corresponding to the same instant as plotted in figure 4. The fields are normalised with corresponding r.m.s. values.

wall ensures its suitability for analysing near-wall turbulence dynamics in the intended application.

The error field, which quantifies the difference between the reference DNS and the corresponding prediction obtained from the FCN, is shown in figure 16 for V predictions and in figure 17 for E predictions and V-E predictions. Overall, the magnitude of the error distributed across the fields increases as the target wall-normal position increases (see also Guastoni *et al.* 2021). Additionally, the pattern and distribution of the error exhibit qualitative differences across various wall-normal positions in the V predictions, although some similarities are observed in the error patterns for the polymeric-stress quantities of interest for E predictions. Moreover, the error fields for V-E predictions are closer to the reference fields of interest, indicating that the network model struggles to capture a range of scales effectively.

Appendix B. Effects of low-pass filtering the velocity fluctuations on prediction of polymeric shear stress

A sample instantaneous field of the polymeric shear stress ($\tau_{p,\,\mathrm{xy}}$) in the test dataset is shown in figure 18(*a*). The sampled DNS field at different wall-normal locations serves as a reference, while the corresponding predictions obtained from FCN with respective inputs at different cutoff wavelengths are depicted. The figure shows that the resulting predictions from FCN lack certain small-scale features with increasing λ_c^+ for different wall-normal locations, a fact that is attributed to the absence of fine-scale features in the input fields.

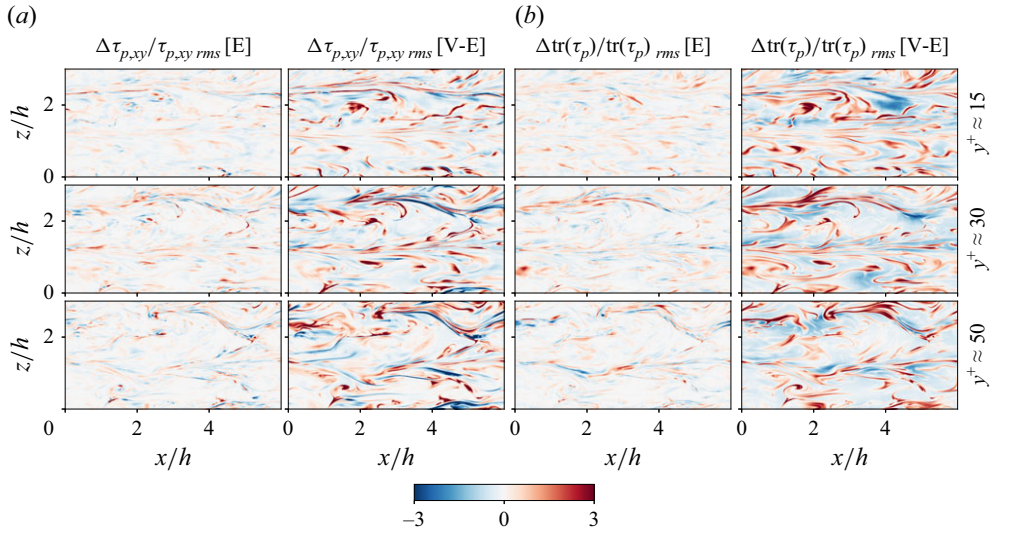

Figure 17. Error fields corresponding to E predictions and V-E predictions of (*a*) polymeric shear stress and (*b*) trace of polymeric stress at different target wall-normal positions, corresponding to the same instant as plotted in figure 6. The fields are normalised with corresponding r.m.s. values.

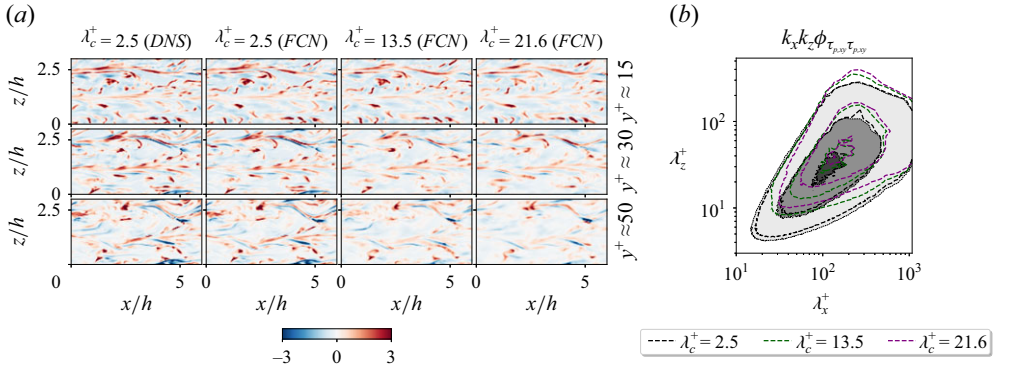

Figure 18. (*a*) A sample polymeric-shear-stress-fluctuation field is plotted at different-wall-normal locations with corresponding predictions from FCN using inputs with different cutoff wavelength of the velocity-fluctuation fields. The fields are scaled with the respective r.m.s. values. (*b*) Pre-multiplied two-dimensional power-spectral density of polymeric shear stress at $y^+ \approx 30$. The contour levels contain 10 %, 50 % and 80 % of the maximum power spectral density. Shaded contours refer to DNS data, while contour lines indicate the cutoff wavelength in the input velocity fluctuations provided to FCN.

Further, the distribution of energy in different scales for both the DNS- and the FCN-predicted polymeric-shear-stress field at $y^+ \approx 30$ is illustrated in figure 18(*b*), which also identifies that the resulting predictions from FCN increasingly feature energy-containing large-scale structures and lack energy content in small scales with increasing λ_c^+.

Appendix C. Joint probability density function of polymeric shear stress

A similar observation can be made for the prediction of the polymeric shear stress with respect to turbulent shear stress as outlined in § 3.6 for the trace of polymeric stress.

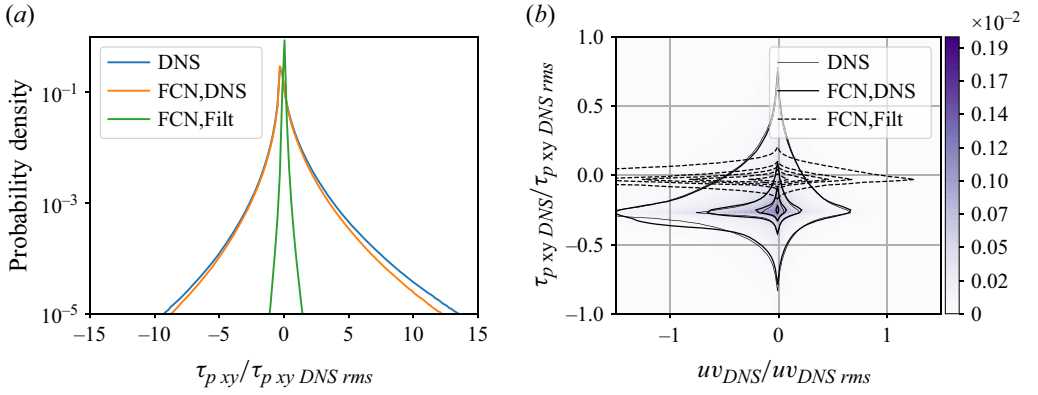

Figure 19. (*a*) Probability density function of the r.m.s.-normalised polymeric shear stress at $y^+ \approx 30$, identifying the distribution of the percentage of data-points in the test dataset with a bin size of 0.18. (*b*) Normalised joint probability density function between turbulent shear stress and polymeric shear stress obtained from DNS samples in the test dataset at $y^+ \approx 30$ and FCN predictions using DNS velocity fluctuations (FCN,DNS) and filtered velocity fluctuations (FCN,Filt) with $\lambda_c^+ = 21.6$.

The probability density function for the r.m.s.-normalised polymeric shear stress is shown in figure 19(*a*). The predictions from FCN using DNS input velocity fluctuations closely capture the probability density function observed with the DNS polymeric-shear-stress fields in the test dataset. However, using the filtered velocity-fluctuation fields with $\lambda_c^+ = 21.6$ results in the distribution of the data being closer to the mean value, indicating an under-prediction of the fluctuations of the polymeric shear stress.

From figure 19(*b*), observing the distribution from DNS samples, we find the polymeric shear stress mitigates the production of turbulent shear stress. Furthermore, predictions of polymeric shear stress using filtered fields are under-predicted, especially in regions with negligible turbulent shear stress. Filtering the input fields alters the Reynolds shear stress, leading to increased errors in the predictions of polymeric shear stress.

References

Beneitez, M., Page, J., Dubief, Y. & Kerswell, R.R. 2024 Transition route to elastic and elasto-inertial turbulence in polymer channel flows. *Phys. Rev. Fluids* **9** (12), 123302.

Beneitez, M., Page, J. & Kerswell, R.R. 2023 Polymer diffusive instability leading to elastic turbulence in plane Couette flow. *Phys. Rev. Fluids* **8** (10), L101901.

Casciola, C.M. & de Angelis, E. 2007 Energy transfer in turbulent polymer solutions. *J. Fluid Mech.* **581**, 419–436.

Couchman, M.M.P., Beneitez, M., Page, J. & Kerswell, R.R. 2024 Inertial enhancement of the polymer diffusive instability. *J. Fluid Mech.* **981**, A2.

Cremades, Aés, Hoyas, S., Deshpande, R., Quintero, P., Lellep, M., Lee, W.J., Monty, J.P., Hutchins, N., Linkmann, M., Marusic, I. & Vinuesa, R. 2024 Identifying regions of importance in wall-bounded turbulence through explainable deep learning. *Nat. Commun.* **15** (1), 3864.

De Gennes, P.G. 1986 Towards a scaling theory of drag reduction. *Physica A Stat. Mech. Appl.* **140** (1-2), 9–25.

Den Toonder, J.M.J., Hulsen, M.A., Kuiken, G.D.C. & Nieuwstadt, F.T.M. 1997 Drag reduction by polymer additives in a turbulent pipe flow: numerical and laboratory experiments. *J. Fluid Mech.* **337**, 193–231.

Dubief, Y., Page, J., Kerswell, R.R., Terrapon, V.E. & Steinberg, V. 2022 First coherent structure in elasto-inertial turbulence. *Phys. Rev. Fluids* **7** (7), 073301.

Dubief, Y., Terrapon, V.E. & Hof, B. 2023 Elasto-inertial turbulence. *Annu. Rev. Fluid Mech.* **55** (1), 675–705.

DUBIEF, Y., TERRAPON, V.E., WHITE, C.M., SHAQFEH, E.S.G., MOIN, P. & LELE, S.K. 2005 New answers on the interaction between polymers and vortices in turbulent flows. *Flow Turbul. Combust.* **74** (4), 311–329.

DUBIEF, Y., WHITE, C.M., TERRAPON, V.E., SHAQFEH, E.S.G., MOIN, P. & LELE, S.K. 2004 On the coherent drag-reducing and turbulence-enhancing behaviour of polymers in wall flows. *J. Fluid Mech.* **514**, 271–280.

EIVAZI, H., GUASTONI, L., SCHLATTER, P., AZIZPOUR, H. & VINUESA, R. 2021 Recurrent neural networks and Koopman-based frameworks for temporal predictions in a low-order model of turbulence. *Intl J. Heat Fluid Flow* **90**, 108816.

EIVAZI, H., TAHANI, M., SCHLATTER, P. & VINUESA, R. 2022 Physics-informed neural networks for solving Reynolds-averaged Navier–Stokes equations. *Phys. Fluids* **34** (7), 075117.

EIVAZI, H., WANG, Y. & VINUESA, R. 2024 Physics-informed deep-learning applications to experimental fluid mechanics. *Meas. Sci. Technol.* **35** (7), 075303.

FATTAL, R. & KUPFERMAN, R. 2004 Constitutive laws for the matrix-logarithm of the conformation tensor. *J. Non-Newtonian Fluid Mech.* **123** (2-3), 281–285.

GRAHAM, M.D. 2014 Drag reduction and the dynamics of turbulence in simple and complex fluids. *Phys. Fluids* **26** (10), 101301.

GUASTONI, L., GÜEMES, A., IANIRO, A., DISCETTI, S., SCHLATTER, P., AZIZPOUR, H. & VINUESA, R. 2021 Convolutional-network models to predict wall-bounded turbulence from wall quantities. *J. Fluid Mech.* **928**, A27.

GUASTONI, L., RABAULT, J., SCHLATTER, P., AZIZPOUR, H. & VINUESA, R. 2023 Deep reinforcement learning for turbulent drag reduction in channel flows. *Eur. Phys. J. E* **46** (4), 27.

HAMEDUDDIN, I., GAYME, D.F. & ZAKI, T.A. 2019 Perturbative expansions of the conformation tensor in viscoelastic flows. *J. Fluid Mech.* **858**, 377–406.

HAMEDUDDIN, I., MENEVEAU, C., ZAKI, T.A. & GAYME, D.F. 2018 Geometric decomposition of the conformation tensor in viscoelastic turbulence. *J. Fluid Mech.* **842**, 395–427.

HAMEDUDDIN, I. & ZAKI, T.A. 2019 The mean conformation tensor in viscoelastic turbulence. *J. Fluid Mech.* **865**, 363–380.

IZBASSAROV, D., ROSTI, M.E., BRANDT, L. & TAMMISOLA, O. 2021 Effect of finite Weissenberg number on turbulent channel flows of an elastoviscoplastic fluid. *J. Fluid Mech.* **927**, A45.

KIM, K., ADRIAN, R.J., BALACHANDAR, S. & SURESHKUMAR, R. 2008 Dynamics of hairpin vortices and polymer-induced turbulent drag reduction. *Phys. Rev. Lett.* **100** (13), 134504.

KIM, K., LI, C.-F., SURESHKUMAR, R., BALACHANDAR, S. & ADRIAN, R.J. 2007 Effects of polymer stresses on eddy structures in drag-reduced turbulent channel flow. *J. Fluid Mech.* **584**, 281–299.

KINGMA, D.P. & BA, J. 2015 Adam: A method for stochastic optimization. In Proc. 3rd International Conference on Learning Represenations (ICLR).

KUMAR, M., GUASTO, J.S. & ARDEKANI, A.M. 2023 Lagrangian stretching reveals stress topology in viscoelastic flows. *Proc. Natl Acad. Sci. USA* **120** (5), e2211347120.

KUMAR, M., CONSTANTE-AMORES, C.R. & GRAHAM, M.D. 2025 Elastoinertial turbulence: Data-driven reduced-order model based on manifold dynamics. *J. Fluid Mech.* **1007**, R1.

LE CLAINCHE, S., IZBASSAROV, D., ROSTI, M.E., BRANDT, L. & TAMMISOLA, O. 2020 Coherent structures in the turbulent channel flow of an elastoviscoplastic fluid. *J. Fluid Mech.* **888**, A5.

LI, C.-F., SURESHKUMAR, R. & KHOMAMI, B. 2006 Influence of rheological parameters on polymer induced turbulent drag reduction. *J. Non-Newtonian Fluid Mech.* **140** (1-3), 23–40.

LI, W. & GRAHAM, M.D. 2007 Polymer induced drag reduction in exact coherent structures of plane Poiseuille flow. *Phys. Fluids* **19** (8), 083101.

LUMLEY, J.L. 1969 Drag reduction by additives. *Annu. Rev. Fluid Mech.* **1** (1), 367–384.

NAGAMACHI, A. & TSUKAHARA, T. 2019 Predictability study of viscoelastic turbulent channel flow using deep learning. In Fluids Engineering Division Summer Meeting, pp. V002T02A077. American Society of Mechanical Engineers.

NEKKANTI, A. & SCHMIDT, O.T. 2021 Frequency–time analysis, low-rank reconstruction and denoising of turbulent flows using SPOD. *J. Fluid Mech.* **926**, A26.

NGUYEN, M.Q., DELACHE, A., SIMOËNS, S., BOS, W.J.T. & EL HAJEM, M. 2016 Small scale dynamics of isotropic viscoelastic turbulence. *Phys. Rev. Fluids* **1** (8), 083301.

PINHO, F.T. & WHITELAW, J.H. 1990 Flow of non-Newtonian fluids in a pipe. *J. Non-Newtonian Fluid Mech.* **34** (2), 129–144.

PTASINSKI, P.K., BOERSMA, B.J., NIEUWSTADT, F.T.M., HULSEN, M.A., VAN DEN BRULE, B.H.A.A. & HUNT, J.C.R. 2003 Turbulent channel flow near maximum drag reduction: simulations, experiments and mechanisms. *J. Fluid Mech.* **490**, 251–291.

PTASINSKI, P.K., NIEUWSTADT, F.T.M., VAN DEN BRULE, B.H.A.A. & HULSEN, M.A. 2001 Experiments in turbulent pipe flow with polymer additives at maximum drag reduction. *Flow Turbul. Combust.* **66** (2), 159–182.

RAIOLA, M., DISCETTI, S. & IANIRO, A. 2015 On PIV random error minimization with optimal POD-based low-order reconstruction. *Exp. Fluids* **56** (4), 1–15.

RAISSI, M., YAZDANI, A. & KARNIADAKIS, G.E. 2020 Hidden fluid mechanics: learning velocity and pressure fields from flow visualizations. *Science* **367** (6481), 1026–1030.

ROSTI, M.E., IZBASSAROV, D., TAMMISOLA, O., HORMOZI, S. & BRANDT, L. 2018 Turbulent channel flow of an elastoviscoplastic fluid. *J. Fluid Mech.* **853**, 488–514.

SHEN, Z., CARRILLO, J.-M.Y., SUMPTER, B.G. & WANG, Y. 2022 Fingerprinting Brownian motions of polymers under flow. *Phys. Rev. Lett.* **129** (5), 057801.

STONE, P.A. & GRAHAM, M.D. 2003 Polymer dynamics in a model of the turbulent buffer layer. *Phys. Fluids* **15** (5), 1247–1256.

STONE, P.A., WALEFFE, F. & GRAHAM, M.D. 2002 Toward a structural understanding of turbulent drag reduction: nonlinear coherent states in viscoelastic shear flows. *Phys. Rev. Lett.* **89** (20), 208301.

SURESHKUMAR, R. & BERIS, A.N. 1995 Effect of artificial stress diffusivity on the stability of numerical calculations and the flow dynamics of time-dependent viscoelastic flows. *J. Non-Newtonian Fluid Mech.* **60** (1), 53–80.

SURESHKUMAR, R., BERIS, A.N. & HANDLER, R.A. 1997 Direct numerical simulation of the turbulent channel flow of a polymer solution. *Phys. Fluids* **9** (3), 743–755.

THAKUR, S., RAISSI, M. & ARDEKANI, A.M. 2024 Viscoelasticnet: a physics informed neural network framework for stress discovery and model selection. *J. Non-Newtonian Fluid Mech.* **330**, 105265

VALENTE, P.C., DA SILVA, C.B. & PINHO, F.T. 2014 The effect of viscoelasticity on the turbulent kinetic energy cascade. *J. Fluid Mech.* **760**, 39–62.

VIGNON, C., RABAULT, J. & VINUESA, R. 2023 Recent advances in applying deep reinforcement learning for flow control: perspectives and future directions. *Phys. Fluids* **35** (3), 031301.

VINUESA, R. 2024 Perspectives on predicting and controlling turbulent flows through deep learning. *Phys. Fluids* **36** (3), 031401.

VINUESA, R. & BRUNTON, S.L. 2022 Enhancing computational fluid dynamics with machine learning. *Nat. Comput. Sci.* **2** (6), 358–366.

VINUESA, R., BRUNTON, S.L. & MCKEON, B.J. 2023 The transformative potential of machine learning for experiments in fluid mechanics. *Nat. Rev. Phys* **5** (9), 536–545.

VIRK, P.S. 1971 Drag reduction in rough pipes. *J. Fluid Mech.* **45** (2), 225–246.

WARHOLIC, M.D., HEIST, D.K., KATCHER, M. & HANRATTY, T.J. 2001 A study with particle-image velocimetry of the influence of drag-reducing polymers on the structure of turbulence. *Exp. Fluids* **31** (5), 474–483.

WARHOLIC, M.D., MASSAH, H. & HANRATTY, T.J. 1999 Influence of drag-reducing polymers on turbulence: effects of Reynolds number, concentration and mixing. *Exp. Fluids* **27** (5), 461–472.

WATANABE, T. & GOTOH, T. 2014 Power-law spectra formed by stretching polymers in decaying isotropic turbulence. *Phys. Fluids* **26** (3), 035110.

WEI, T. & WILLMARTH, W.W. 1992 Modifying turbulent structure with drag-reducing polymer additives in turbulent channel flows. *J. Fluid Mech.* **245**, 619–641.

XI, H.-D., BODENSCHATZ, E. & XU, H. 2013 Elastic energy flux by flexible polymers in fluid turbulence. *Phys. Rev. Lett.* **111** (2), 024501.

XI, L. 2019 Turbulent drag reduction by polymer additives: fundamentals and recent advances. *Phys. Fluids* **31** (12), 121302.

XI, L. & GRAHAM, M.D. 2010 Active and hibernating turbulence in minimal channel flow of Newtonian and polymeric fluids. *Phys. Rev. Lett.* **104** (21), 218301.

XI, L. & GRAHAM, M.D. 2012 Intermittent dynamics of turbulence hibernation in Newtonian and viscoelastic minimal channel flows. *J. Fluid Mech.* **693**, 433–472.

XU, Z.-Q.J., ZHANG, Y. & XIAO, Y. 2019 Training behavior of deep neural network in frequency domain. In *NeurIPS* (eds. GEDEON, T., WONG, K.W. & LEE, M.), pp. 264–274. Springer International Publishing.

YERASI, S.R., PICARDO, J.R., GUPTA, A. & VINCENZI, D. 2024 Preserving large-scale features in simulations of elastic turbulence. *J. Fluid Mech.* **1000**, A37.

YOUSIF, M.Z., YU, L., HOYAS, S., VINUESA, R. & LIM, H. 2023*a* A deep-learning approach for reconstructing 3D turbulent flows from 2D observation data. *Sci. Rep.* **13** (1), 2529.

YOUSIF, M.Z., ZHANG, M., YU, L., VINUESA, R. & LIM, H. 2023*b* A transformer-based synthetic-inflow generator for spatially developing turbulent boundary layers. *J. Fluid Mech.* **957**, A6.

YOUSIF, M.Z., ZHANG, M., YU, L., YANG, Y., ZHOU, H. & LIM, H. 2023*c* Physics-constrained deep reinforcement learning for flow field denoising. *J. Fluid Mech.* **973**, A12.